


# Dielectric Relaxation Mechanism in the Phase-Transition Region of a Chiral Hybrid Perovskite and Its Piezoelectric-Energy-Harvesting Properties

Aditi Sahoo<sup>1</sup>, Tufan Paul<sup>1</sup>, Pulak Pal<sup>2</sup>, Nisha Hiralal Makani<sup>1</sup>, Aswini Ghosh<sup>2,\*</sup> and Rupak Banerjee<sup>1,3,†</sup>

<sup>1</sup>Department of Physics, Indian Institute of Technology Gandhinagar, Palaj 382355, India

<sup>2</sup>School of Physical Sciences, Indian Association for the Cultivation of Science, Jadavpur, Kolkata 700032, India

<sup>3</sup>K C Patel Centre for Sustainable Development, Indian Institute of Technology Gandhinagar, Palaj, Gandhinagar 382355, India

 (Received 9 May 2023; revised 23 June 2023; accepted 18 August 2023; published 12 September 2023)

Chiral halide perovskites are being extensively studied due to their promising spintronic and optoelectronic properties, where the organic chiral ligands introduce chirality into halide perovskites. Right-handed and left-handed chiral materials are mirror images of one another and break the inversion symmetry, which produces ferroelectricity. In this work, we study the dielectric, piezoelectric, and ferroelectric properties of  $(R)$ -(-)-1-cyclohexylethylammonium $\text{PbI}_3$  ( $R$ -CYHEAPbI<sub>3</sub>), a chiral, one-dimensional perovskite. We performed and analyzed complex impedance spectroscopy; ac conductivity; and the complex electric modulus using the Maxwell-Wagner equivalent circuit model, the universal power law, the Havriliak-Negami (HN) model, and the Kohlrausch-Williams-Watts (KWW) model to understand the transport and relaxation mechanism in the chiral  $R$ -CYHEAPbI<sub>3</sub> perovskite over wide temperature (313–473 K) and frequency (4 Hz–8 MHz) ranges. The dc conductivity is almost constant in the paraelectric-to-ferroelectric phase-transition region (PTR) but increases below and above this region. The activation energy of this region is very low, about 0.09 eV, while below the PTR, the activation energy is about 0.85 eV, and above the PTR, it is about 0.90 eV. We further note that the conduction mechanism changes from overlapped large polaron tunneling to correlated barrier hopping due to the ferroelectric-to-paraelectric phase transition. The activation energy derived from the relaxation time (using HN and KWW models) agrees with that obtained from the dc conductivity. In addition, we measured the saturation polarization of 0.01  $\mu\text{C}/\text{cm}^2$  at a 4-kV/cm applied electric field and a piezoelectric constant ( $d_{33}$ ) of about 36 pm/V at the maximum applied bias voltage of 10 V. Finally, we fabricated a polyvinylidene fluoride and 3-wt%  $R$ -CYHEAPbI<sub>3</sub> chiral perovskite composite film for the development of high-performance energy-harvesting nanogenerators.

DOI: [10.1103/PhysRevApplied.20.034024](https://doi.org/10.1103/PhysRevApplied.20.034024)

## I. INTRODUCTION

Recently, organic-inorganic halide perovskites have attracted much attention due to their optoelectronic; ferroelectric; piezoelectric; photocatalytic; energy harvesting; and, most importantly, photovoltaic properties [1–9]. The band gap and electrical behavior are controlled by the lead and iodine octahedra of hybrid perovskites and create suitable semiconducting attributes with strong spin-orbit coupling, whereas the organic groups act as chemical and structural stabilizers. The variety of organic groups allows the exploration of functionalities such as ferroelectricity and chirality, while still ensuring the desired semiconducting characteristics [10]. Chiral materials have widespread use in the field of asymmetric

catalysis [11], optoelectronic devices [12], biology [13], information communication [14], and many more. The incorporation of chirality into metal-halide semiconductors is desired to obtain an alternative class of chiral semiconducting material, mainly by incorporating chiral organic molecules into metal-halide lattices. Excitons and charge carriers in chiral metal halides show a high spin-polarization response due to inversion-symmetry breaking and improved spin-orbit coupling [15]. The single crystal of a chiral metal-halide semiconductor (CMHS) was first reported by Billing *et al.* in methyl benzylamine (known as MBA) [16]. This was followed by a report on a single crystal of a two-dimensional CMHS [17]. The chiroptical phenomenon in  $[R(S)$ -MBA]<sub>2</sub>PbI<sub>4</sub> [ $R$ - ( $S$ -) refers to the clockwise or right-handed (counterclockwise or left-handed) chiral enantiomer], reported by Ahn *et al.*, triggered great interest in CMHSs [18]. Incorporating a chiral organic molecule into a metal-halide perovskite introduces

\*sspaga@iacs.res.in

†rupakb@iitgn.ac.in

chiral lattice defects [19], the design of chiral metasurfaces [15,20], and blends with chiral matrices. (*R*)-(-)-1-Cyclohexylethylamine (*R*-CYHEA,  $C_8H_{15}NH_2$ ) and (*S*)-(+)-1-cyclohexylethylamine (*S*-CYHEA,  $C_8H_{15}NH_2$ ) are two organic chiral groups that make *R*-CYHEAPbI<sub>3</sub> and *S*-CYHEAPbI<sub>3</sub> chiral metal-halide perovskites, where *R* and *S* stands for right-handed and left-handed chirality [10]. These *R*-CYHEAPbI<sub>3</sub> and *S*-CYHEAPbI<sub>3</sub> compounds are electrically switchable photoferroelectric semiconductors [10]. Here, the organic groups are responsible for chirality and ferroelectricity by eliminating mirror and inversion symmetry, respectively, from the PbI<sub>6</sub> octahedra, which control the band structure and transport characteristics of the material. First-principles calculations, density measurements, and x-ray diffraction (XRD) characterization indicate that *R*-CYHEAPbI<sub>3</sub> and *S*-CYHEAPbI<sub>3</sub> remain in the space group  $P2_1$  with an angle of  $\beta = 89.5121^\circ$  [10] at room temperature. Hu *et al.* [10] reported that a phase transition occurred at around 100 °C, where these chiral ferroelectric materials entered the paraelectric phase by switching to the orthorhombic space group  $P2_12_12_1$ . Cai *et al.* [21] demonstrated how this *R*-CYHEAPbI<sub>3</sub>, which was a ferroelectric van der Waals halide perovskite, could be used to simulate synaptic activity. The influence of ferroelectric polarization switching on the photovoltaic response of two-terminal photoferroelectric synapses was also reported by Cai *et al.* [22].

To increase the effectiveness of electrical and optoelectronic devices, researchers have focused on the synthesis and optoelectronic characterization of metal-halide perovskite materials [23]. However, a complete understanding of the electrical transport mechanism and the dielectric behavior of *R*-CYHEAPbI<sub>3</sub> is still lacking [24]. Consequently, comprehensive knowledge of the frequency-dependent dielectric properties and conduction mechanism of *R*-CYHEAPbI<sub>3</sub> is imperative. Dielectric spectroscopy extensively explores the ac conduction mechanism and dielectric relaxation over a wide frequency range and at various temperatures. Various dielectric properties, such as complex impedance, dielectric permittivity, electrical modulus, and ac conductivity, can be investigated by dielectric spectroscopy measurements. The presence or absence of the relaxation peak in the modulus plots can distinguish the long-range and short-range conduction processes of the materials. The activation energy and the relaxation behavior often indicate the predominant transport mechanism in the materials. The behavior of the dielectric parameters was previously investigated for characterizing a diverse set of materials, including conducting polymers, ceramics, transition-metal oxides, and halide perovskites, to understand and correlate the conduction and relaxation mechanisms with their ferroelectric and piezoelectric properties [25].

The dielectric attributes of chiral perovskites are still unexplored because quantitative work on this aspect is

relatively scarce. The properties of the localized charge carriers, the conduction mechanism, the permittivity, the loss factor, etc. can all be thoroughly explained by the temperature- and frequency-dependent dielectric analysis of *R*-CYHEAPbI<sub>3</sub>. There have been no extensive studies of the dielectric relaxation and ac conductivity of *R*-CYHEAPbI<sub>3</sub> chiral hybrid perovskite. Here, we synthesized *R*-CYHEAPbI<sub>3</sub> using the wet chemical method and studied its dielectric and piezoelectric properties. The experimental dielectric spectroscopic data were fitted to different theoretical models, such as the Maxwell-Wagner equivalent circuit model, the universal power law, the Havriliak-Negami (HN) model, and the Kohlrausch-Williams-Watts (KWW) model. We observed that the dc conductivity was weakly temperature dependent over the temperature range 353–373 K, but the dc conductivity increased with temperature below and above this temperature range. This anomaly in the dc conductivity was attributed to the ferroelectric-to-paraelectric phase transition. The activation energy in this region is extremely low ( $\sim 0.09$  eV). In contrast, the activation energy is an order of magnitude higher ( $\sim 0.85$  eV) below the phase-transition region (PTR) as well as ( $\sim 0.90$  eV) above the PTR. The activation energies calculated using the HN and KWW models from the relaxation time plots agree well with the value obtained via dc conductivity plots. The scaling of temperature-dependent conductivity and electric modulus spectra into a single master curve demonstrates the consistency of the ionic conduction and relaxation phenomena for *R*-CYHEAPbI<sub>3</sub> at different temperatures. Chiral *R*-CYHEAPbI<sub>3</sub> displays a piezoelectric constant ( $d_{33}$ ) of 36 pm/V at the maximum applied bias voltage of 10 V and a saturation polarization of 0.01  $\mu\text{C}/\text{cm}^2$  at an applied electric field of 4 kV/cm. Finally, we prepared a composite film by loading 3-wt% *R*-CYHEAPbI<sub>3</sub> chiral perovskite into polyvinylidene fluoride (PVDF) matrix and demonstrated its mechanical energy-harvesting properties.

## II. EXPERIMENT

### A. Chemicals

Lead iodide (PbI<sub>2</sub>), *R*-CYHEA, hydriodic acid (HI), dimethylformamide (DMF), PVDF pellets ( $M_w$  approx. 275 000 g/mol) were purchased from Sigma-Aldrich, USA, and acetone was purchased from Merck Chemicals, India. All of these chemicals were utilized without further purification.

### B. *R*-CYHEAPbI<sub>3</sub> synthesis

Chiral *R*-CYHEAPbI<sub>3</sub> was synthesized under an ambient atmosphere. 0.125 mmol of PbI<sub>2</sub> and 5 mmol of *R*-CYHEA were mixed in a 3 ml aqueous solution of HI acid in a round-bottomed flask. Next, the entire mixture was stirred for 2 h at 150 °C using a silicon oil bath. After

that, the temperature was slowly lowered to room temperature at a cooling rate of 2 °C/h. Then the precipitate was centrifuged at 7000 rpm with isopropyl alcohol to eliminate excess and impurity materials. Finally, the collected sample was dried overnight at 90 °C in a vacuum oven.

### C. PVDF and *R*-CYHEAPbI<sub>3</sub> composite-film preparation

0.5 g PVDF pellets were added to the acetone (4 ml) and DMF (3 ml) mixture. Afterward, 20 mg of as-synthesized chiral *R*-CYHEAPbI<sub>3</sub> was added to the above solution and stirred for 2 h at 70 °C. A yellow-colored homogeneous solution was obtained and then drop cast onto precleaned glass slides. These coated substrates were kept under vacuum at 70 °C overnight. Thereafter, films were peeled off from the glass slides and used for device fabrication and various characterization techniques.

## III. CHARACTERIZATION

For structural characterization, first, we performed powder XRD using a 9-kW multimode XRD system (Smart-Lab, Rigaku Corp., Japan). The copper  $K\alpha$  (wavelength,  $\lambda = 1.54 \text{ \AA}$ ) was used as a source with a  $2\theta$  range from 5° to 60°. The scan rate was maintained at 1°/min. Field-emission scanning electron microscopy was employed for the microstructural and elemental analysis of the as-prepared sample (JEOL JSM-7900F). X-ray photoelectron spectroscopic (XPS) analysis was carried out by using a NEXA base ThermoFisher Scientific XPS instrument to find the elemental composition and the oxidation states of the individual elements of the chiral one-dimensional (1D) *R*-CYHEAPbI<sub>3</sub> perovskite. UV-visible reflectance spectroscopy was performed by using a QE-R quantum efficiency measurement system (EnliTech, Taiwan). Thermogravimetric analysis (TGA) and differential scanning calorimetry (DSC) of *R*-CYHEAPbI<sub>3</sub> were performed using a Perkin Elmer TGA analyzer and a Perkin Elmer differential scanning calorimeter, respectively.

To perform the dielectric spectroscopic measurements, *R*-CYHEAPbI<sub>3</sub> powder was pressed into a pellet and placed in a two-electrode configuration setup. The dielectric measurements were carried out via an LCR spectrometer (HIOKI, model IM 3536) in the frequency range of 4 Hz–8 MHz with a perturbation potential of 1 V and a temperature range of 313–473 K. Piezoelectric force microscopy (PFM) was performed by using an Asylum Research AFM (MFP-3D BIO) by applying an ac bias voltage (10 V) to investigate the local piezoresponse properties by operating in contact mode. The RADIANT ferroelectric test apparatus (Radiant Technologies Inc.) and Vision software were used to perform the room-temperature ferroelectric measurements. A digital oscilloscope (YOKOGAWA, DL 1640) was used to investigate the piezoelectric characteristics of PVDF and the composite films during

mechanical energy harvesting from biomechanical movements.

## IV. RESULTS AND DISCUSSION

### A. Structural study

To confirm the phase purity and crystallinity of the as-prepared sample, first, we carried out XRD measurements. The XRD profile of as-prepared *R*-CYHEAPbI<sub>3</sub> perovskite is shown in Fig. 1(a), with distinct intense peaks at 7.66°, 10.60°, 15.25°, 18.91°, 24.14°, 25.72°, 26.94°, 27.87°, and 42.89°, which correspond to the (002), (101), (004), (005), (−212), (−213), (124), (116), and (026) planes, respectively. As-prepared *R*-CYHEAPbI<sub>3</sub> belongs to the monoclinic lattice system and chiral  $P2_1$  space group [10]. We performed the Le Bail profile fitting using FullProf software and determined the lattice parameters of our material, which were  $a = 8.75 \text{ \AA}$ ,  $b = 8.44 \text{ \AA}$ ,  $c = 23.46 \text{ \AA}$ , and  $\beta = 89.08^\circ$ . The sample showed remarkable phase purity, and no impurity peaks were observed. Hu *et al.* [10] reported the finer structural details of *R*-CYHEAPbI<sub>3</sub> using first-principles density-functional-theory calculations. These calculations show that opposite rotations of the amine groups on either side of the (001) plane break the inversion symmetry along the  $b$  direction, giving rise to polarization in the structure [10], due to which *R*-CYHEAPbI<sub>3</sub> is a chiral ferroelectric at room temperature. Figure 1(b) shows the time-dependent XRD data of our synthesized material. We performed the x-ray diffraction of *R*-CYHEAPbI<sub>3</sub> immediately after synthesizing the material and after six months of ambient storage. The XRD patterns in both cases are identical, indicating that the material is stable for at least six months. The energy-dispersive spectroscopy (EDX) data demonstrate that the elemental compositions of the particles constitute only Pb, I, N, and C [Fig. 1(c)] and no other impurity elements. From the TGA and derivative thermogravimetry (DTG) measurements shown in Fig. 1(d), we note that the *R*-CYHEAPbI<sub>3</sub> sample is thermally stable up to 250 °C. The fastest weight loss happens from 310 °C, as seen in Fig. 1(d). To demonstrate the phase change, a DSC measurement was also performed (Fig. S1 within the Supplemental Material [26]). As can be seen, a phase transition is indicated by a sharp peak in the DSC heating and cooling curves at about 85 and 98 °C, respectively. Hu *et al.* reported the DSC peak at 100 °C [10], which was quite close to that observed in our study. The minor difference may be attributed to the reduced size of the particles in our case. The peaks in the FTIR spectrum [Fig. 1(e)] show the formation of N—H bonds and C—H bonds at around 3200 and 2900  $\text{cm}^{-1}$ , respectively, in the organic cation group *R*-CYHEA. XPS analysis was performed to check the chemical composition of *R*-CYHEAPbI<sub>3</sub> perovskites and to assess the oxidation states of constituent elements. UV-visible spectroscopic measurement was deployed to determine

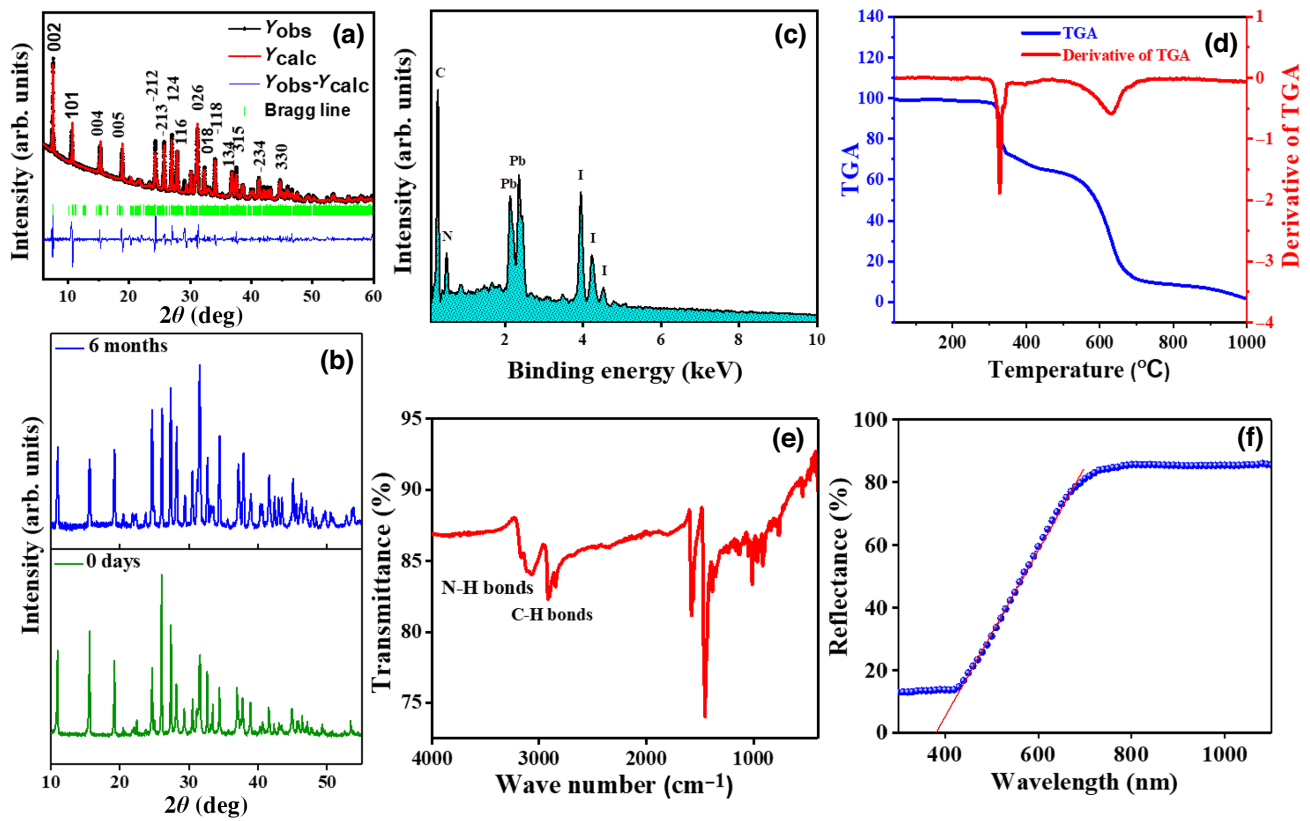


FIG. 1. (a) XRD profile along with its refinement, (b) stability for six months, (c) EDX profile, (d) TGA and DTG, (e) FTIR spectrum, and (f) reflectance spectrum of the  $R$ -CYHEAPbI<sub>3</sub> 1D chiral halide perovskite.

the band-gap energy of the as-synthesized perovskite sample. The diffuse reflectance spectrum is shown in Fig. 1(f), where reflectance is plotted as a function of the photon wavelength,  $\lambda$  (nm), and the estimated band-gap value is 3.23 eV.

In the deconvoluted spectrum of C 1s in Fig. 2(a), two peaks at 286.05 and 284.5 eV are observed. The higher binding energy peak of C 1s is from the C—N bond in the  $R$ -CYHEA cation. The lower-binding-energy peak is attributed to adventitious carbon, and it is not related to the perovskite itself. The binding energies of carbon peaks are consistent with previous reports [27,28]. Figure 2(b) shows the N 1s peak at 400.6 eV [29]. XPS spectra of Pb and I are presented in Figs. 2(c) and 2(d). Pb 4*f* and I 3*d* both exhibit typical doublet features of Pb and I, respectively. The peaks corresponding to Pb 4*f*<sub>5/2</sub> and Pb 4*f*<sub>7/2</sub> states are at about 142.7 and 137.8 eV, respectively [30]. The peaks ascribed to I 3*d*<sub>3/2</sub> and I 3*d*<sub>5/2</sub> states are positioned at about 630.5 and 619.05 eV, respectively. Figure S2 within the Supplemental Material [26] shows the XPS survey spectra of carbon (C), nitrogen (N), lead (Pb), and iodine (I).

## B. Impedance analysis

Complex impedance spectroscopy is a significant and well-recognized technique for examining the electrical

response of materials. It provides ionic mobilities, relaxation time, electrical conductivity, etc. inside the material. We measured the impedance spectra over the temperature range of 313–473 K to investigate the charge-carrier transport processes and dielectric relaxation mechanism in the chiral  $R$ -CYHEAPbI<sub>3</sub> perovskites. The impedance spectroscopic measurement was performed over the range of 4 Hz–8 MHz. Figure 3(a) shows the variation of the real component of impedance [ $Z'(\omega)$ ] with frequency ( $\omega$ ) over the temperature range 313–473 K. The correlation between the real part of impedance with frequency reveals that, as frequency increases, the impedance value decreases because grain boundaries contribute less to the total impedance at higher frequencies. We noticed that, in low-frequency regions, resistance decreased as temperature and frequency increased, indicating a negative temperature coefficient [31]. The conductance thus increases with temperature due to an increase in charge-carrier mobility and a decrease in the trapped-charge density inside the perovskites.

It is interesting to note that  $Z'(\omega)$  showed a negative coefficient for  $dZ'/dT$  below a certain frequency and a positive coefficient for  $dZ'/dT$  beyond this frequency. Figure 3(b) shows the variation of the imaginary part of impedance [ $Z''(\omega)$ ] with frequency over the temperature range 313–473 K, which is also known as the “loss spectrum.” These plots are essential for an in-depth



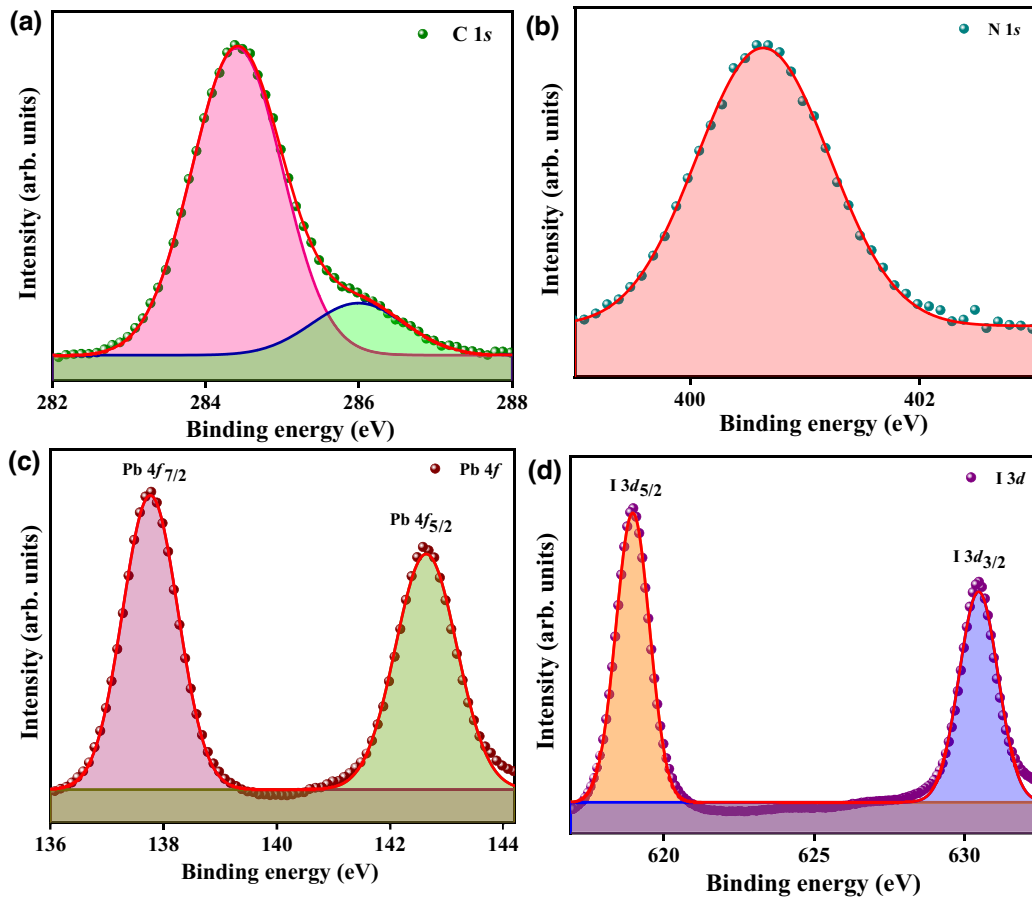


FIG. 2. XPS results for (a) C 1s, (b) N 1s, (c) Pb  $4f_{7/2}$  and Pb  $4f_{5/2}$ , and (d) I  $3d_{5/2}$  and I  $3d_{3/2}$  of  $R$ -CYHEAPbI<sub>3</sub> 1D chiral halide perovskite.

understanding of the charge-transport mechanism and relaxation behavior of  $R$ -CYHEAPbI<sub>3</sub> perovskites as a function of temperature. Every spectrum has a clearly defined distinctive peak, which is referred to as the “relaxation frequency.” This relaxation peak appears when the applied-field frequency matches the hopping frequency of the charge carriers. It is also noteworthy that the broadness in the peaks indicates deviation from the ideal Debye nature. The charge carriers exhibit long-range motion below the relaxation frequency and undergo short-range motion above the same. The shifting of relaxation peaks towards high frequency with increasing temperature suggests a thermally activated relaxation mechanism. Moreover, the reduction in the peak value of relaxation frequency with rising temperature indicates a decrease in the grain and grain-boundary resistances and an increase in charge-storage capacity or capacitance [32,33]. The relaxation frequency and relaxation time versus temperature are plotted in Fig. 3(c). The relaxation time decreases and the relaxation frequency increases with rising temperature, suggesting the thermally activated relaxation mechanism of  $R$ -CYHEAPbI<sub>3</sub> perovskites [34]. Additionally, we observed three distinct regions, the first below 353 K,

defined as the LTR, and the last above 373 K, defined as the HTR, separated by an intermediate (353–373 K range), which was identified as the PTR. Our DSC results corroborate this phase transition, which was also observed earlier by Hu *et al.* [10]. These three distinct temperature regions are also identifiable in the rest of the plots. Furthermore, we calculated the activation energy of charge-carrier relaxation following the Arrhenius equation

$$\tau = \tau_0 \exp\left(\frac{E_a}{k_B T}\right), \quad (1)$$

where  $\tau_0$  is defined as the relaxation time,  $E_a$  is defined as the activation energy, and  $k_B$  is the Boltzmann constant. The activation energies estimated from the slopes in Fig. 3(d) are  $0.85(\pm 0.04)$  eV below 353 K in the LTR,  $0.1(\pm 0.04)$  eV in the PTR, and  $0.95(\pm 0.04)$  eV beyond 373 K in the HTR. These values of activation energy play a significant role in the hopping mechanism of charge carriers in the lattice sites, which we elucidate later in the ac conductivity section (Sec. IV D).

Figures 4(a)–4(c) display the real part of complex impedance [ $Z'(\omega)$ ] versus the imaginary component of

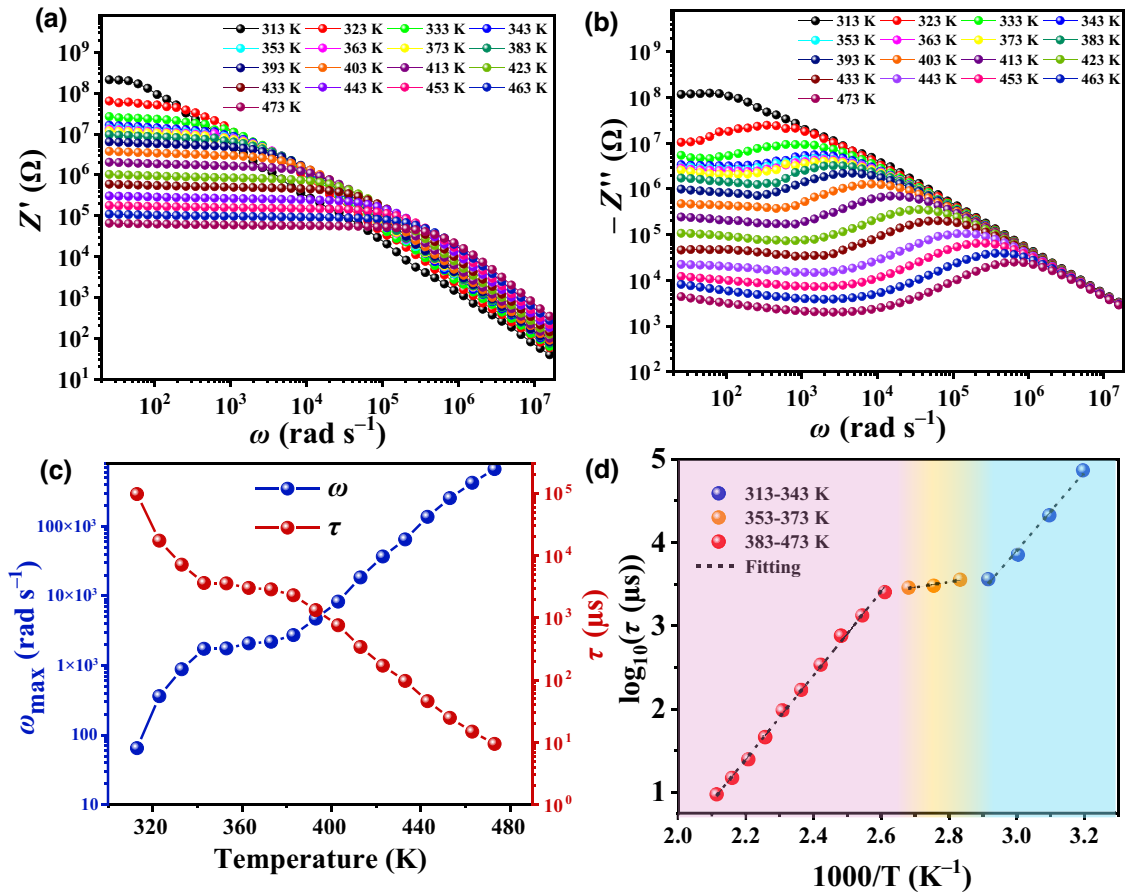


FIG. 3. (a) Frequency-dependent real part of impedance ( $Z'$ ) and (b) frequency-dependent imaginary part of impedance ( $Z''$ ) over the temperature range 313–473 K. (c) Variation in the peak position of frequency ( $\omega_{\max}$ ) for  $Z''$  and relaxation time ( $\tau$ ) with temperature. (d) Arrhenius plots in the low-temperature region (LTR), phase transition region (PTR), and the high-temperature region (HTR). The LTR, PTR, and HTR are shown in different shades.

impedance [ $Z''(\omega)$ ] at various temperatures. This curve is frequently referred to as the Nyquist plot or the Cole-Cole plot. In the Nyquist diagram, any dielectric material will usually have three different semicircles that represent the contribution of the grain, grain boundary, and electrode-material interface to the total impedance of the dielectric material. The grain contributes to the semicircles that appear in the high-frequency region, whereas the material's grain boundaries contribute to those in the low-frequency region. Finally, the semicircle in the ultralow-frequency zone is the contribution from the sample-electrode interface [35]. The entire impedance spectra of the sample over the temperature range of 313–473 K are shown in Figs. 4(a)–4(c), and each of them essentially exhibits a semicircular arc. These arcs consist of three semicircles emanating from the grain, grain boundary, and the sample-electrode surface, and it is nontrivial to differentiate the actual contribution from each. To estimate the contribution of these grain and grain boundaries distinctly from the semicircular arc, we invoke the Maxwell-Wagner

equivalent circuit model, which consists of three parallel combinations [shown in insets of Figs. 4(a)–4(c)] of resistance ( $R$ ) and constant phase element (CPE), which is defined by the following relationship [36]:

$$Z_{\text{CPE}} = \frac{1}{A(j\omega)^n} \quad (2)$$

Here,  $A$  stands for a proportionality factor;  $\omega$  indicates the applied angular frequency; and  $n$  is an exponent between 0 and 1, when the CPE shifts from being an ideal resistor ( $n=0$ ) to a perfect capacitor ( $n=1$ ) [37]. The Nyquist plots indicate that the radius of the semicircle decreases with increasing temperature. A decrease in the real axis intercept implies conductivity enhancement with increasing temperature. The complex impedance is given by

$$Z(\omega) = Z'(\omega) - jZ''(\omega). \quad (3)$$

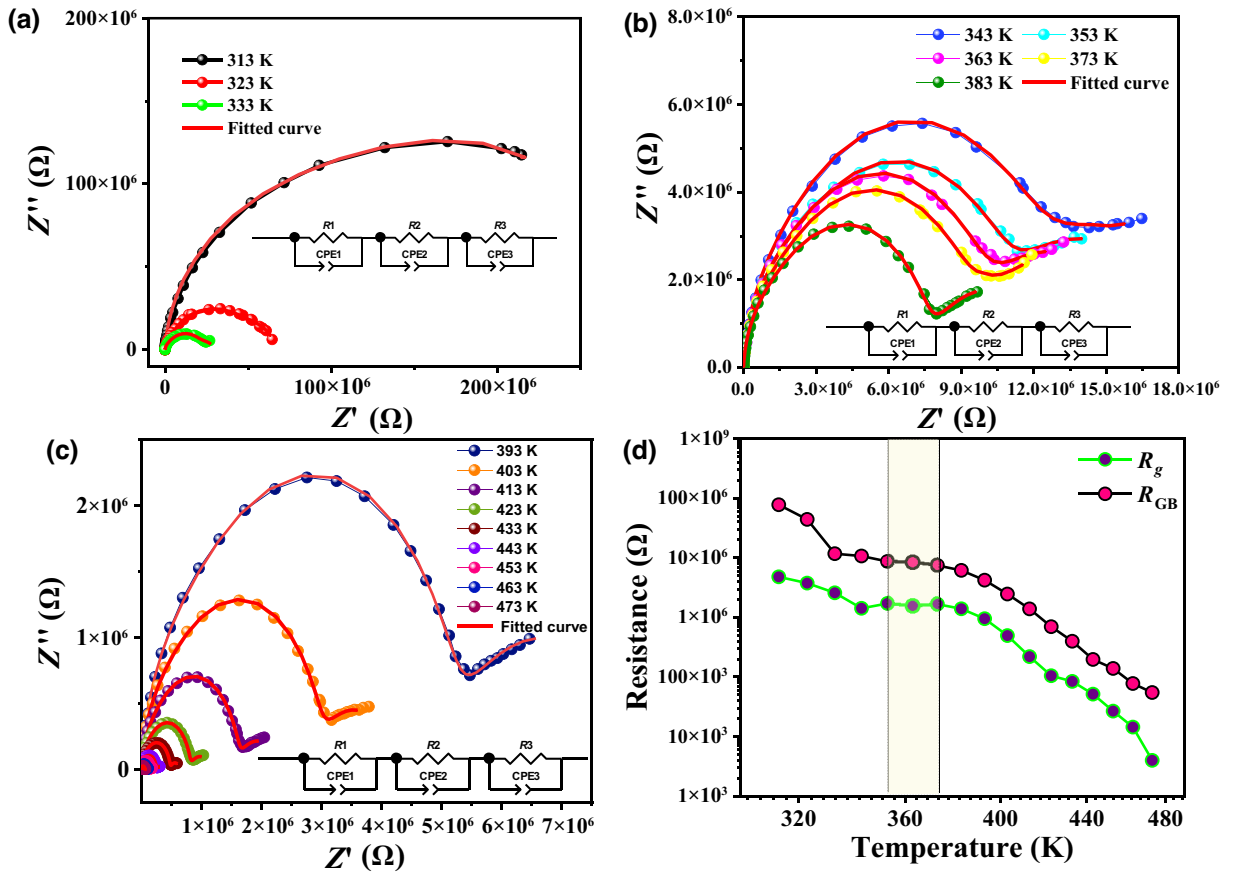


FIG. 4. Complex plane Nyquist plots of  $R$ -CYHEAPbI<sub>3</sub> nanoparticles in the range (a) 313–333 K, (b) 343–383 K, and (c) 393–473 K. Insets show the equivalent circuit model used to fit data. (d) Variations in the resistances  $R_g$  and  $R_{GB}$  over the whole temperature range are extracted from fitting the data. Shaded region is the phase-transition region.

$Z'(\omega)$  and  $Z''(\omega)$  may be expressed as

$$Z'(\omega) = \frac{R_g}{[1 + (\omega R_g C_g)^2]} + \frac{R_{GB}}{[1 + (\omega R_{GB} C_{GB})^2]}, \quad (4)$$

$$Z''(\omega) = \frac{\omega C_g R_g^2}{[1 + (\omega R_g C_g)^2]} + \frac{\omega C_{GB} R_{GB}^2}{[1 + (\omega R_{GB} C_{GB})^2]}, \quad (5)$$

where  $R_g$  stands for grain resistance,  $C_g$  is the grain capacitance,  $R_{GB}$  is the grain-boundary resistance, and  $C_{GB}$  is the grain-boundary capacitance. All of the resistance and capacitance values obtained from Nyquist-plot fitting for various temperatures are listed in Table S1 within the Supplemental Material [26]. The variation in  $R_g$  and  $R_{GB}$  over the whole temperature range is shown in Fig. 4(d). It is observed that the resistance of the grain and the grain boundary decreases with temperature initially; then remains constant, forming a plateau region; and, after crossing this plateau region, it decreases again with temperature. This implies that the plateau region [shown as the shaded region in Fig. 4(d)] is indeed the

phase-transition region, wherein the  $R$ -CYHEAPbI<sub>3</sub> perovskites transit from the monoclinic ferroelectric to the orthorhombic paraelectric phase.

### C. Analysis of dielectric properties

The dielectric response of any material is given by the complex dielectric constant:

$$\varepsilon(\omega) = \varepsilon'(\omega) - j\varepsilon''(\omega), \quad (6)$$

where  $\varepsilon'(\omega)$  corresponds to the real component of the dielectric constant, representing the stored energy, and  $\varepsilon''(\omega)$  corresponds to the imaginary part of the dielectric constant, indicating energy dissipation in the material. Furthermore, the real and imaginary parts of the dielectric constant can be expressed as

$$\varepsilon'(\omega) = \frac{Z'}{\omega C_0 (Z'^2 + Z''^2)}, \quad (7)$$

$$\varepsilon''(\omega) = \frac{Z''}{\omega C_0 (Z'^2 + Z''^2)}, \quad (8)$$

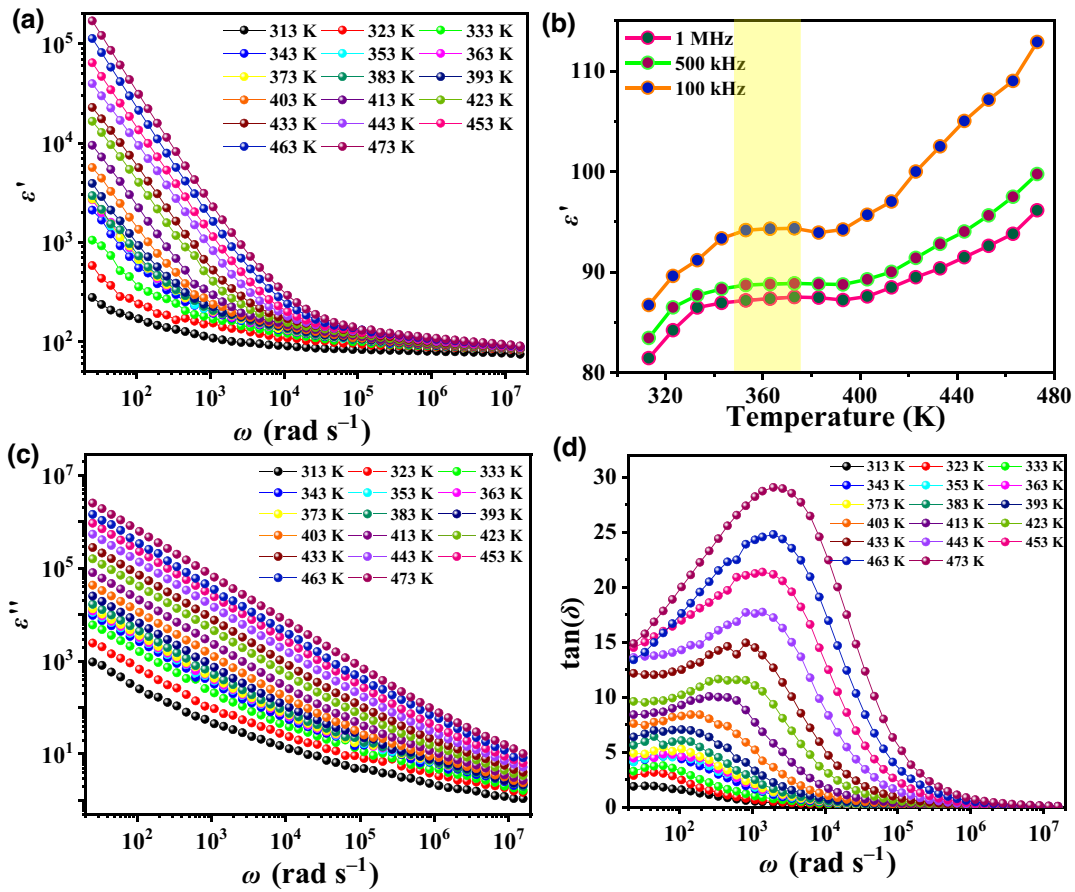


FIG. 5. Frequency-dependent real part of (a) dielectric constant ( $\epsilon'$ ) over the temperature range 313–473 K; (b) temperature-dependent dielectric constant at fixed frequencies of 100 kHz, 500 kHz, and 1 MHz; and (c) frequency-dependent dielectric loss ( $\epsilon''$ ) and (d) loss tangent ( $\tan\delta$ ) at different temperatures for the *R*-CYHEAPbI<sub>3</sub> nanoparticles.

$$\tan \delta = \frac{\epsilon''}{\epsilon'} = \frac{Z''}{Z'}, \quad (9)$$

where  $C_0 = \epsilon_0 A/d$ ;  $C_0$  represents the capacitance of free space,  $\epsilon_0$  represents the permittivity of free space,  $A$  is the area of the electrode, and  $d$  is the thickness of the pellet. The variation of  $\epsilon'(\omega)$ ,  $\epsilon''(\omega)$ , and  $\tan \delta$  with frequency is investigated over the temperature range of 313–473 K. Figure 5(a) shows the frequency-dependent real part of the dielectric constant over a temperature range of 313–473 K. The value of  $\epsilon'(\omega)$  is higher at low-frequency regions and decreases gradually with an increase in frequency.  $\epsilon'(\omega)$  plays a crucial role in ionic conductivity, as it depends on one or more of the four main types of polarization, namely, ionic, electronic, orientational, and interfacial polarization. While the orientational and interfacial polarizations are represented by the relaxation component of polarizability, the ionic and electronic polarizations correspond to the deformational component of polarizability [38].

The Maxwell-Wagner interfacial polarization helps us to understand the variation in the real component of permittivity with frequency, which is consistent with

Koop's phenomenological theory [39,40]. In this model, it is assumed that, in the material, the grain with a lower resistance is separated by the grain boundary with a higher resistance. The charge carriers are trapped in the interface of the grain boundary to reduce their flow so that dielectric loss is lowered [41]. The interfacial polarization process involves an exchange of electrons between ions of the same molecules. However, the position and distribution of positive and negative space charges are altered due to deformities and flaws in the material. When the electric field is applied to the material, positive and negative charges shift towards the negative and positive poles of the applied electric field, respectively, and create a large number of dipoles [40,42]. The material has a high dielectric constant at low frequencies ( $\omega \ll 1/\tau$ ) because the dipoles can easily follow the quasistatic field at these frequencies. The dielectric constants gradually decrease in the high-frequency region as the dipoles lose their ability to follow the electric field at higher frequencies. Thus, the electronic and ionic polarizations dominate in the high-frequency domain, whereas the orientational and interfacial polarizations contribute more (to the real part



of the dielectric constant) in the low-frequency domain, accounting for the lower values of  $\varepsilon'(\omega)$ . Additionally, at a particular frequency, the values of  $\varepsilon'(\omega)$  increase as the temperature is raised, indicating the presence of thermally activated charge carriers in this phenomenon. Figure 5(b) shows the change of  $\varepsilon'(\omega)$  with the temperature at three different frequencies (100 kHz, 500 kHz, and 1 MHz). The entire  $\varepsilon'(\omega)$ - $T$  pattern has three prominent features: (i) LTR (313–343 K), which is below the phase-transition region; (ii) PTR (353–373 K), where the ferroelectric-to-paraelectric phase transition occurs; and (iii) HTR (383–473 K), which is above the phase-transition region. In the LTR,  $\varepsilon'(\omega)$  increases with temperature, while in the PTR  $\varepsilon'(\omega)$  becomes almost temperature independent [as observed in the shaded part in Fig. 5(b)]; this may be because of the high entropy associated with the system in the phase-transition regime [43]. The entropy enhancement decreases the dipole's capability to orient along the applied field. In the HTR,  $\varepsilon'(\omega)$  again starts to rise with temperature. Additionally, we investigate the frequency-dependent behavior of dielectric loss [ $\varepsilon''(\omega)$ ] over the temperature range of 313–473 K, which is shown in Fig. 5(c). For a particular temperature, it is noted that the dielectric loss factor decreases with increasing frequency. According to Koop's theory, any impurity or defect in a material can act as a barrier to the movement of charge carriers [39]. The space-charge polarization prevents the partial conduction of charges until they get blocked at a potential barrier or grain boundary. The effect of the grain boundary is dominant in the low-frequency region, reducing the ability of electrons to hop and enhancing the dielectric loss. At high frequencies, the less-resistive grains become prominent, and the hopping electrons are unable to follow the applied electric field. Thus, a small amount of energy is needed to transfer electrons between the ions of the same molecules, resulting in low dielectric losses. As mentioned earlier, while all four different types of polarization occur in the low-frequency region, only ionic and electronic polarizations dominate in the high-frequency region. This reduces the dielectric loss factor in the high-frequency region over the temperature range of 313–473 K [44,45]. The value of dielectric loss rises as temperature increases because it is a thermally activated process.

The loss tangent represents the ratio of the imaginary to the real part of the dielectric constant. The variation in the loss tangent with frequency over the temperature range of 313–473 K is shown in Fig. 5(d). The loss tangent at a particular temperature shows two zones: first, the loss tangent increases with frequency until it reaches a maximum value, and second, beyond the maximum value, it decreases with an increase in frequency. The loss peak appears when the hopping frequency matches the frequency of the applied external ac field. In the LTR, the loss peaks appear in the low-frequency region due to the predominant dipolar polarization. As the temperature increases, the loss-tangent

value rises, and the peaks shift towards the high-frequency region, demonstrating that dipolar polarization is a thermally controlled process.

#### D. Frequency-dependent ac conductivity

The variation of ac conductivity as a function of frequency over the temperature range of 313–473 K is depicted in Fig. 6(a). It is observed that the ac conductivity is frequency independent up to a particular frequency (called the “hopping frequency”), and beyond this frequency, the conductivity increases with frequency. The conductivity estimated in the low-frequency region, which is mainly frequency independent, is attributed to the dc conductivity. At high frequencies, however, the conductivity follows a frequency dispersion mainly attributed to the ac conductivity. At low frequencies, activated hopping results in random diffusion of charge carriers, creating the dc conductivity ( $\sigma_{dc}$ ), while, in the frequency-dispersive region, ions move in a correlated forward-backward motion.

This frequency-independent dc and frequency-dependent ac conductivity can be interpreted by the jump-relaxation model proposed by Funke and Hoppe [46]. Once an ion hops out and leaves its stable configuration, it does not necessarily revert to an equilibrium position with its neighbors. If the neighboring ions reconfigure to accommodate this ion in a stable position, it is termed “successful hopping.” However, if the ion assumes a nonequilibrium position with respect to its neighbors, it goes back to its initial configuration to salvage a partially relaxed arrangement, thus exhibiting a “forward-backward jump” or an “unsuccessful hopping” [37]. The conductivity at low frequencies is mainly attributed to successful hops, which facilitate long-range ionic translational motion. The ratio of successful-to-unsuccessful hopping determines the dispersion in the conductivity spectra. The high-frequency region depicts more unsuccessful hops and, consequently, higher dispersion. The ac conductivity curve is fitted using the Jonscher power law [47–49]:

$$\sigma_{ac}(\omega) = \sigma_{dc} + A\omega^s, \quad (10)$$

where  $\sigma_{dc}$  is the dc conductivity of the material;  $A$  is the preexponential factor;  $\omega$  represents the angular frequency; and  $s$  is the power-law exponent, which is representative of how the mobile ions interact with their surrounding lattices ( $0 < s < 1$ ) [50].

$\sigma_{dc}$  is obtained from the fitting of the Jonscher power law for all temperatures and is observed to follow the Arrhenius relationship:

$$\sigma_{dc} = \sigma_0 \exp\left(-\frac{E'_a}{k_B T}\right), \quad (11)$$

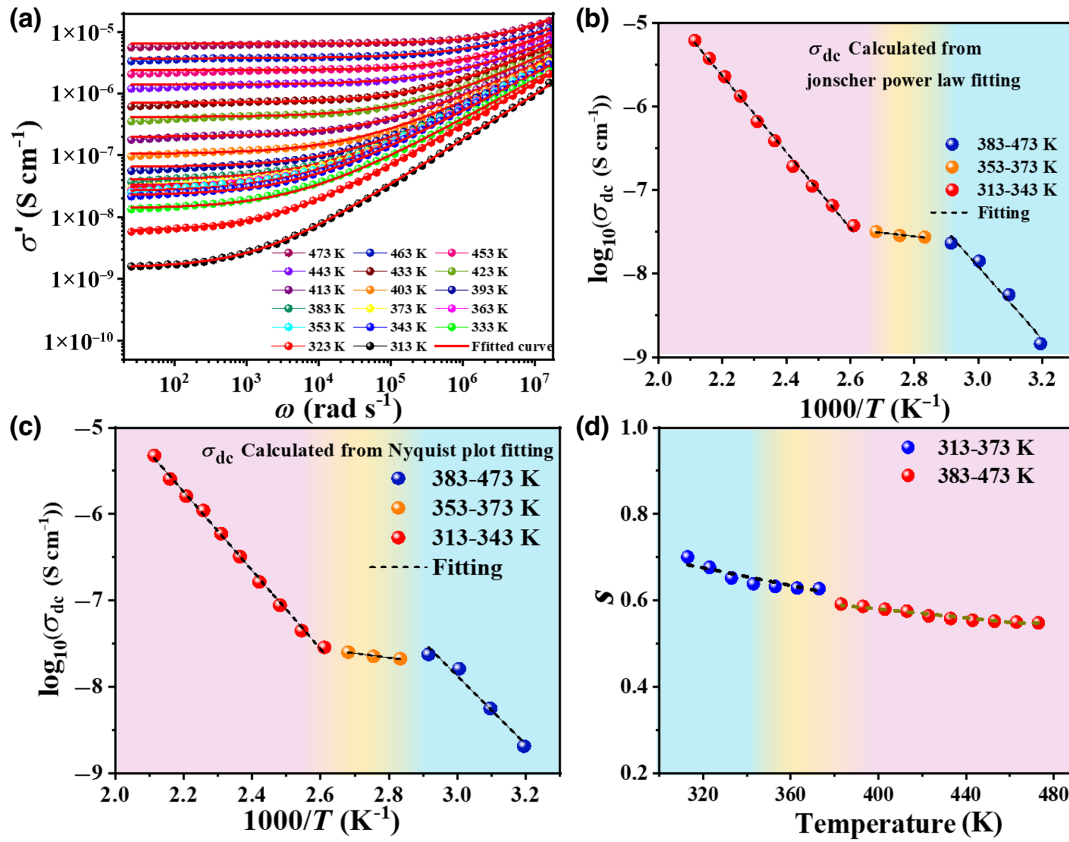


FIG. 6. (a) Frequency-dependent ac conductivity at different temperatures (313–473 K); (b)  $\sigma_{dc}$  versus  $1000/T$  plot; (c)  $\sigma_{dc}$  versus  $1000/T$  plot obtained from the complex impedance plot, showing Arrhenius behavior in the LTR, PTR, and HTR shown in different shades. (d) Frequency exponent ( $s$ ) as a function of temperature. Dashed lines are fits corresponding to the OLPT model in the LTR and PTR but the CBH model in the HTR.

where  $\sigma_0$  is the preexponential factor,  $E'_a$  represents the activation energy,  $k_B$  is the Boltzmann constant, and  $T$  is the absolute temperature. To find the activation energy of the conduction process, we plot  $\sigma_{dc}$  versus  $1000/T$ , as shown in Fig. 6(b). We obtain three activation energies using straight-line fits, which correspond to  $0.85(\pm 0.04)$ ,  $0.09(\pm 0.04)$ , and  $0.90(\pm 0.04)$  eV for the LTR, PTR, and LTR, respectively. These values are close to the activation energies obtained from the imaginary part of the impedance ( $Z''$ ) curve. We have also calculated the dc conductivity ( $\sigma_{dc}$ ) of the material at different temperatures from the fitted Nyquist plots by using the relationship  $\sigma_{dc} = t/RA$ , where  $R$  is the total resistance ( $R = R_g + R_{GB} + R_e$ ),  $t$  is the thickness, and  $A$  is the sample area. The dc conductivity measured from the complex impedance at various temperatures is displayed in Fig. 6(c). It is worth mentioning that the value of  $\sigma_{dc}$  derived from power-law fits of the ac conductivity, and the calculated activation energies precisely match the values estimated from complex impedance data.

Notably, the dc conductivity in the PTR does not vary too much with increasing temperature. We observe a much lower activation energy (1 order of magnitude less than the

activation energies in the LTR and the HTR) required for conduction. The charge carriers consequently move in the lattice more efficiently. In the PTR, the ions break bonds spontaneously, increasing the disorder and entropy in the transition region, which reduces the activation energy. The material reaches the paraelectric phase at higher temperatures, resulting in a higher symmetric phase. Consequently, it needs more energy to delocalize charge carriers or break bonds to create charge carriers. The activation energy is, therefore, larger in the HTR than the activation energy of the ferroelectric phase in the LTR.

We invoke theoretical models that describe the temperature dependence of the frequency exponent ( $s$ ) to understand the ac conduction mechanism in the chiral material  $R$ -CYHEAPbI<sub>3</sub> [51,52]. Although halide perovskites are mixed ionic and electronic conductors [35], the inherent lattice distortions induce polaronic behavior of electrons, as indicated in Fig. 6(d), which demonstrates the change in the frequency exponent ( $s$ ) with temperature. The four models, which have been used predominantly to describe the ac conduction mechanism in different classes of materials, are (i) the correlated barrier-hopping (CBH) model, (ii) the nonoverlapping small-polaron tunneling

(NSPT) model, (iii) the overlapping large-polaron tunneling (OLPT) model, and (iv) the quantum mechanical tunneling (QMT) model. We have identified the relevant model(s) applicable to our chiral perovskite material based on the frequency-exponent ( $s$ ) behavior with temperature. While for the CBH model  $s$  decreases with increasing temperature, for the NSPT model,  $s$  increases with increasing temperature. Furthermore, for the OLPT model, the exponent  $s$  drops with temperature to a minimal value and then slowly increases, and finally, for the QMT model, the value of the exponent parameter,  $s$ , is about 0.81, and it is temperature independent. In our case, exponent  $s$  decreases initially with temperature and then increases to a certain value (313–373 K); however, after the phase transition, it decreases with temperature. In the ferroelectric phase, it follows the OLPT model (in the temperature range of 313–373 K), and in the paraelectric phase, it follows the CBH model (in the temperature range of 383–473 K) [51,53–55].

The polaron-tunneling mechanism in the OLPT model assumes overlapping of the polaron distortion clouds. The spatial extent of the large polaronic clouds is essentially larger than the interatomic distance spacing, often leading to the overlap of adjacent potential wells. As a result, the polaron-hopping energy decreases, since the activation energy associated with the motion of charge carriers between sites follows [54,55]

$$W_H = W_{H0} \left(1 - \frac{r_p}{R}\right), \quad (12)$$

where  $r_p$  is the polaron radius,  $R$  is the distance between interstitial sites, and  $W_H$  is the polaron-hopping energy [53,54].  $W_{H0}$  is expressed as

$$W_{H0} = \frac{e^2}{4\epsilon_p r_p}. \quad (13)$$

$\epsilon_p$  is the effective dielectric constant, and, for the OLPT model,  $W_{H0}$  is expected to be a constant for all sites. The ac conductivity can then be written as

$$\sigma_{ac} = \frac{\pi^4 e^2 k_B^2 T^2 \omega N(E_F)^2 R_\omega^4}{12(2\alpha k_B T + W_{H0} r_p / R_\omega^2)}, \quad (14)$$

where  $T$  is the temperature,  $k_B$  is the Boltzmann constant,  $N(E_F)$  is the density of states at the Fermi level, and  $\alpha^{-1}$  denotes the spatial extension of the polaron wave function. The hopping length ( $R_\omega$ ) is calculated as follows:

$$R_\omega^2 + (\beta W_{H0} + \ln(\omega \tau_0)) R_\omega' - \beta W_{H0} r_p' = 0, \quad (15)$$

where  $R_\omega' = 2\alpha R_\omega$ ,  $\beta = 1/k_B T$ , and  $r_p' = 2\alpha r_p$ . The frequency exponent for  $s$  in the OLPT model thus becomes

[51,53–55]

$$s = 1 - \frac{8\alpha R_\omega + (6W_{H0} r_p / R_\omega k_B T)}{[2\alpha R_\omega + (W_{H0} r_p / R_\omega k_B T)]^2}. \quad (16)$$

The theoretical approach of the OLPT model fits well with the experimental data, as shown in Fig. 6(d). The fitting parameters are calculated using Eqs. (12), (13), (15), and (16) and presented in Table S2 within the Supplemental Material [26].

In the CBH model, the ac conductivity over a narrow energy-range limit is expressed as

$$\sigma(\omega) = \frac{\pi^3}{12} N^2 \epsilon \epsilon_0 \omega R_\omega^6, \quad (17)$$

where  $N$  is the concentration of pair sites and  $R_\omega$  is the hopping distance given by

$$R_\omega = \frac{2e^2}{\pi \epsilon \epsilon_0 [W_M + k_B T \ln(\omega \tau_0)]}, \quad (18)$$

with  $W_M$  being the height of binding energy, and  $\tau_0$  being the characteristic relaxation time.

The frequency exponent,  $s$ , for this model is evaluated as [50]

$$s = 1 - \frac{6k_B T}{W_M + k_B T \ln(\omega \tau_0)}, \quad (19)$$

which, to a first approximation, reduces to the simple expression

$$s = 1 - \frac{6k_B T}{W_M}. \quad (20)$$

It should be mentioned that, for the single-electron CBH model, Eqs. (17) and (18) are multiplied by 1/2. Equation (19), however, remains unaltered. The fitting parameters calculated using Eqs. (18) and (19) are shown in Table S3 within the Supplemental Material [26].

### E. Complex modulus spectroscopy

We have investigated the relaxation mechanism of  $R$ -CYHEAPbI<sub>3</sub> perovskites by analyzing the electric modulus spectra. The complex electric modulus is represented as  $M^*(\omega)$ , which is the reciprocal of complex dielectric permittivity,  $\epsilon^*(\omega)$  [56]:

$$M^*(\omega) = \frac{1}{\epsilon^*(\omega)} = \frac{1}{\epsilon' - j\epsilon''} = \frac{\epsilon'}{\epsilon'^2 + \epsilon''^2} + j \frac{\epsilon''}{\epsilon'^2 - \epsilon''^2} = M'(\omega) + jM''(\omega), \quad (21)$$

where  $M'(\omega)$  and  $M''(\omega)$  are the real and imaginary parts, respectively, of complex electric modulus spectra,  $M^*(\omega)$ .

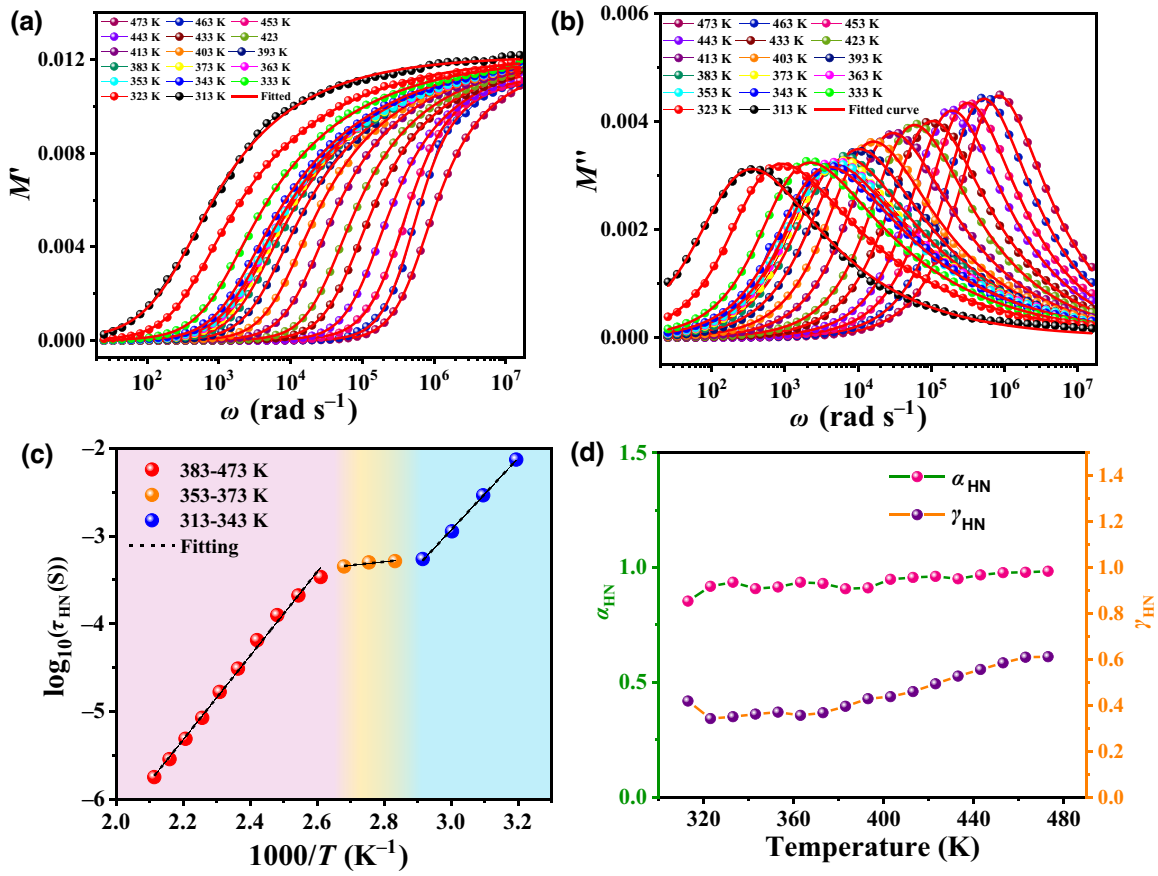


FIG. 7. Variation of (a) real part of the complex electric modulus [ $M'(\omega)$ ] and (b) imaginary part of the complex electric modulus [ $M''(\omega)$ ] with frequency ( $\omega$ ). (c) Relaxation time and reciprocal of the sample temperature show Arrhenius-type behavior with three different slopes, corresponding to the LTR, PTR, and HTR. (d) Variation of  $\alpha_{\text{HN}}$  and  $\gamma_{\text{HN}}$  for the R-CYHEAPbI<sub>3</sub> nanoparticles at different temperatures.

Figures 7(a) and 7(b) display the variation of  $M'(\omega)$  and  $M''(\omega)$ , respectively, with frequency over the temperature range of 313–473 K. Figure 7(a) demonstrates that, for all temperatures, the value of  $M'(\omega)$  is very small at low frequency, gradually rises with frequency, and exhibits a plateaulike characteristic at high frequency. The value of  $M'(\omega)$  is close to zero at low frequency, since the electric field is insufficient for charge flow. After the transition frequency, the hopping of ions takes place with the frequency rise and the value of  $M'(\omega)$  increases. As the temperature increases, the  $M'(\omega)$  curve shifts towards high frequency, which indicates more instances of ion hopping with temperature [57]. The  $M''(\omega)$  spectra exhibit distinct prominent peaks at all temperatures; this is attributed to the material's relaxation frequency. The value of  $M''(\omega)$  increases with frequency and reaches the relaxation frequency. The long-range motion of ions is represented at the left (low-frequency region) and short-range localized motion is represented at the right (high-frequency region) side of the  $M''(\omega)$  versus  $\omega$  curve. This long-range motion takes place when the frequency is low, as the ion gets enough time to hop in the lattice, but, after a particular

frequency, when the time is too short to continue long-range hopping, the ion relaxes and the short-range motion takes over.

When temperature increases, the peaks shift toward high temperatures because of their thermally activated relaxation behavior. The asymmetric relaxation peaks indicate that the relaxation nature of the material is of non-Debye type. To explain the asymmetric nature of peaks, the complex modulus spectra [ $M'(\omega)$  and  $M''(\omega)$ ] are analyzed using the HN model [58], which is expressed as

$$M^*(\omega) = M_{\infty} + \left( \frac{M_S - M_{\infty}}{[1 + (j\omega\tau_{\text{HN}})^{\alpha_{\text{HN}}}]^{\gamma_{\text{HN}}}} \right), \quad (22)$$

where  $M_S$  and  $M_{\infty}$  are the low- and high-frequency limiting values, respectively, of the  $M'(\omega)$ ;  $\tau_{\text{HN}}$  is the relaxation time;  $\alpha_{\text{HN}}$  and  $\gamma_{\text{HN}}$  are the shape parameters with limiting conditions  $0 < \alpha_{\text{HN}}$  or  $\gamma_{\text{HN}} \leq 1$  and  $0 < \alpha_{\text{HN}} \gamma_{\text{HN}} \leq 1$  and represent the symmetric and asymmetric broadening of relaxation peaks. The complex modulus impedance spectra of R-CYHEAPbI<sub>3</sub> at different temperatures are fitted to the real and imaginary parts of Eq. (22) in Figs. 7(a) and 7(b),



respectively. Figure 7(c) shows the plot of relaxation time,  $\tau_{\text{HN}}$ , as a function of the reciprocal of temperature, which obeys Arrhenius behavior:

$$\tau_{\text{HN}} = \tau_0 \exp\left(\frac{E_{\text{HN}}}{k_B T}\right). \quad (23)$$

Similar to previous observations, we also observe three distinct regions in this plot, namely, the LTR, PTR, and HTR. The activation energy calculated from the linear fit in the LTR (313–343 K) is  $E_{\text{HN1}} \sim 0.81(\pm 0.04)$  eV, in the PTR (353–373 K) is  $E_{\text{HN2}} \sim 0.08(\pm 0.04)$  eV, and in the HTR (483–473 K) is  $E_{\text{HN3}} \sim 0.94(\pm 0.04)$  eV; these values are similar to the activation energies calculated from the dc conductivity plots. Figure 7(d) shows the variation of the shape parameters  $\alpha_{\text{HN}}$  and  $\gamma_{\text{HN}}$  as a function of temperature obtained from the best fits of the complex modulus spectra. It indicates that the values of  $\alpha_{\text{HN}}$  are nearly independent of temperature, whereas the values of  $\gamma_{\text{HN}}$  increase slowly with an increase in temperature. The complex modulus spectra are also studied by using the KWW formalism given by [59]

$$M^*(\omega) = M_\infty \left(1 - \int_0^\infty \left(-\frac{d\phi}{dt}\right) e^{-j\omega t} dt\right), \quad (24)$$

where the relaxation function,  $\phi(t)$ , describes the decay of the applied electric field,  $E(t)$ , in the time domain. The

relaxation function,  $\phi(t)$ , can be expressed by the KWW relaxation function:

$$\phi(t) = \exp\left(-\left(\frac{t}{\tau_{\text{KWW}}}\right)^\beta\right), \quad (25)$$

where  $\tau_{\text{KWW}}$  is the KWW relaxation time and  $\beta$  ( $0 < \beta \leq 1$ ) is the stretched exponent [60]. The relaxation function,  $\phi(t)$ , is calculated from the inverse Fourier transform of Eq. (24) given by [61]

$$\phi(t) = \frac{2}{\pi} \int_0^\infty \frac{M''}{\omega M_\infty} \cos(\omega t) d\omega. \quad (26)$$

Figure 8(a) shows the relaxation function,  $\phi(t)$ , derived from the best fit of Eq. (26) to modulus data for  $R\text{-CYHEAPbI}_3$  at various temperatures. Figure 8(b) shows the reciprocal temperature dependence of the KWW relaxation time ( $1/\tau_{\text{KWW}}$ ) derived from the best fit, which follows the Arrhenius relationship [62]. This Arrhenius relationship also gives activation energies of  $0.81(\pm 0.04)$  eV in the LTR,  $0.08(\pm 0.04)$  eV in the PTR, and  $0.94(\pm 0.04)$  eV in the HTR.

#### F. Scaling of conductivity and electric modulus spectra

The temperature dependence of the conduction and relaxation mechanism in  $R\text{-CYHEAPbI}_3$  is investigated

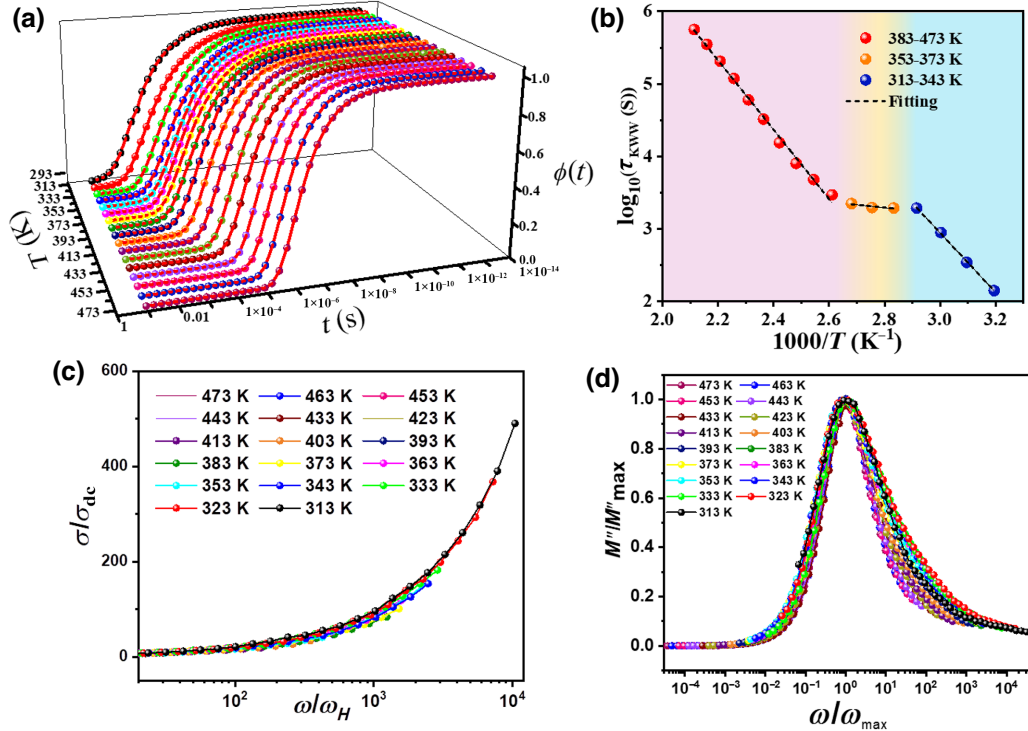


FIG. 8. (a) Plot of time and temperature dependence of  $\phi(t)$ . (b) Reciprocal temperature dependence ( $1000/T$ ) of the KWW relaxation time ( $\tau_{\text{KWW}}$ ), showing three distinct Arrhenius-type behaviors in the LTR, PTR, and HTR. Scaling of (c) the ac conductivity spectra,  $\sigma'(\omega)$ , and (d) the electric modulus loss,  $M''(\omega)$ , at different temperatures for  $R\text{-CYHEAPbI}_3$  perovskites.



using the scaling behavior of the conductivity and complex modulus spectra, as shown in Figs. 8(c) and 8(d). Scaling has been performed based on the formalism reported earlier [63]. The conductivity scaling relationship is given by the scaling formalism:  $\sigma'(\omega)/\sigma_{dc} = F(\omega/\omega_s)$ , where  $F$  is the temperature-independent scaling factor and  $\omega_s$  is the scaling parameter [63]. The scaling results of conductivity at several temperatures for  $R$ -CYHEAPbI<sub>3</sub> are shown in Fig. 8(c).

It is observed that all the conductivity spectra at different temperatures merge into a single master curve. This scaling behavior of the conductivity spectra reveals that  $R$ -CYHEAPbI<sub>3</sub> follows the time-temperature superposition principle. The scaling curve of the electric modulus for this  $R$ -CYHEAPbI<sub>3</sub> is shown in Fig. 8(d), where each

frequency is scaled by the relaxation frequency,  $\omega_{max}$ , and  $M''(\omega)$  is scaled by  $M''_{max}(\omega)$  [maximum value of  $M''(\omega)$ ]. It is observed that the modulus spectra for different temperatures scale on a single master curve, indicating that the dynamic processes are independent of temperature in the  $R$ -CYHEAPbI<sub>3</sub> sample.

### G. Piezoelectric and ferroelectric properties

$R$ -CYHEAPbI<sub>3</sub> is an established ferroelectric material [10], so we perform PFM to observe its piezoelectric behavior. The performance of piezoelectric devices strongly depends on their capability to convert mechanical deformation into electricity, which is determined by the value of its piezoelectric coefficient ( $d_{33}$ ). Figure 9

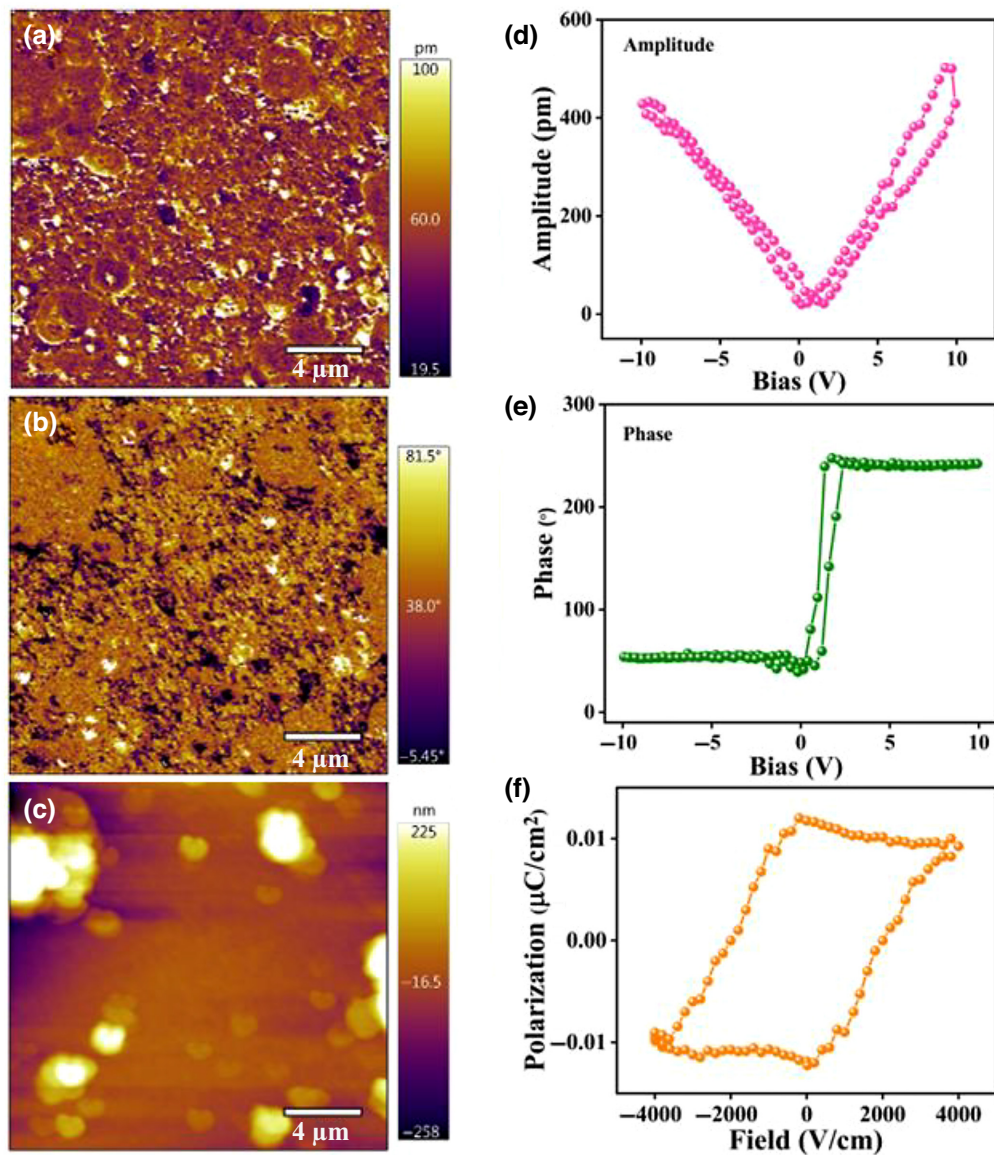


FIG. 9. Piezoelectric force microscopy response: (a) amplitude, (b) phase, (c) topographic image, (d) amplitude butterfly loop, (e) phase hysteresis loop, and (f) polarization versus electric field ( $P$ - $E$ ) loop of the  $R$ -CYHEAPbI<sub>3</sub> perovskites thin film.

illustrates the obtained images of (a) amplitude ( $A$ ), (b) phase ( $^\circ$ ), and (c) topography of the  $R$ -CYHEAPbI<sub>3</sub> perovskites with an active area of  $20 \times 20 \mu\text{m}^2$ . Figures 9(d) and 9(e) show the butterfly-shaped amplitude loop and phase-angle-derived hysteresis loop of the material. In the measurement process, the amplitude and phase loops are obtained under a bias voltage of  $\pm 10$  V. The maximum amplitude of the butterfly loop is about 506 pm. This demonstrates that the sample experiences localized strains (deformations) due to the applied electric field. Similarly, during the applied-bias range of 10 V, the phase changes from  $54^\circ$  to  $240^\circ$ , confirming domain switching under the applied electric field. The piezoelectric coefficient is calculated from the equation  $A_{\text{deflection}} = d_{33}E_{\text{ac}}$  [64]. The calculated value of  $d_{33}$  of the  $R$ -CYHEAPbI<sub>3</sub> perovskites is approximately 36 pm/V, which is comparable to the  $d_{33}$  value of other halide perovskites. The piezoresponse hysteresis loop is calculated using the equation  $P_r(E) = A(E)\cos[\varphi(E)]$  [65,66]. The resulting piezoresponse hysteresis loop of  $R$ -CYHEAPbI<sub>3</sub> perovskites is asymmetric and demonstrated in Fig. S3 within the Supplemental Material [26]. A shift of the loop towards positive bias along the electric field axis suggests that the  $R$ -CYHEAPbI<sub>3</sub> perovskites already have a built-in field that encourages polarization in a particular way. The polarization-electric field ( $P$ - $E$ ) hysteresis loop is obtained in Fig. 9(f) using a Sawyer-Tower circuit, which displays a remanent polarization of about  $0.01 \mu\text{C}/\text{cm}^2$ . To judge

the figure of merit of the synthesized sample, its piezoresponse is compared with other reported values [64,66–71] in Table S4 within the Supplemental Material [26].

### H. Nanogenerator application

In this group of halide perovskites, the ferroelectricity and piezoelectricity emanate due to the large chiral organic group, which removes the mirror and inversion symmetry. To demonstrate the application of this piezoelectric material as a flexible mechanical energy harvester, we prepared a composite film of PVDF and loaded it with 3-wt%  $R$ -CYHEAPbI<sub>3</sub> perovskites. Next, we fabricated two nanogenerator devices, (i) bare PVDF and (ii) PVDF and chiral  $R$ -CYHEAPbI<sub>3</sub> composite, with dimensions of  $5 \times 2 \text{ cm}^2$  to compare the piezoelectric output voltage. The fabrication and encapsulation processes were detailed in our previous work [66]. The nanogenerator fabricated using pristine PVDF is referred to as RNG. The other composite with 3-wt% halide perovskite is referred to as PNG. Figures 10(a) and 10(b) show the instantaneous output voltage and current of two devices fabricated by hand hammering. Here, the PNG shows an output voltage and current of about 65 V and about  $2.74 \mu\text{A}$ , respectively, whereas the RNG shows an output voltage and current of about 25 V and about  $0.76 \mu\text{A}$ , respectively. The higher voltage and current obtained in the PNG may be because of the combined effect of piezoelectricity in

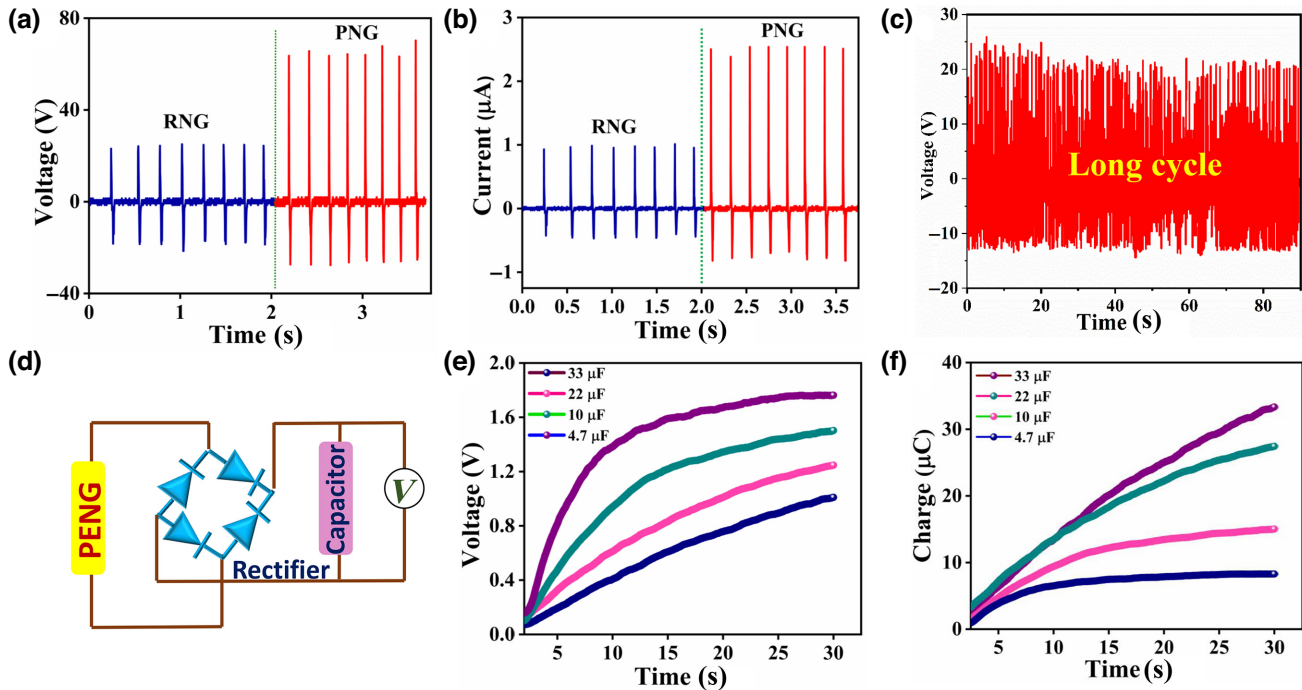


FIG. 10. (a) Output voltage and (b) current from RNG and PNG due to hand hammering. (c) Long cycle performance up to 90 s of PNG due to hand hammering. (d) Schematic diagram of capacitor-charging process using a bridge rectifier. (e) Charging process and (f) corresponding accumulated charges in the four different capacitors.

*R*-CYHEAPbI<sub>3</sub> and the activated beta-phase of PVDF by the addition of perovskite. The output voltage across the PNG up to 90 s is shown in Fig. 10(c), which shows the long-cycle performance of the fabricated nanogenerator. Many devices require high instantaneous output in addition to quick charging-discharging with a high output voltage over a short period of time. In this context, the PNG was connected to a capacitor via a bridge rectifier and subjected to biomechanical action. Figure 10(d) illustrates the capacitor-charging circuit. Figure 10(e) shows the charging of four different capacitors, 4.7, 10, 22, and 33  $\mu$ F, as a function of time. This figure also demonstrates that the 4.7- $\mu$ F capacitor can be fully charged (1.8 V) within 30 s of continuous pressure applied by hand.

The power stored in the capacitor is determined by

$$P_{\text{out}} = \frac{1}{2t} CV^2, \quad (27)$$

where  $P_{\text{out}}$  stands for the power stored;  $C$  is the capacitance of the capacitor. The saturation voltage is  $V$ , and the time it takes to reach that value is  $t$ . So, the power obtained in the 4.7- $\mu$ F capacitor is about 0.25  $\mu$ W. Figure 10(f) shows the calculated charge stored in the 4.7-, 10-, 22-, and 33- $\mu$ F capacitors. These results suggest that the mechanical energy harvester is a potentially useful power source for low-power microelectronic devices. The performance of other nanogenerators is listed in Table S5 within the Supplemental Material [26] for comparison [72–77].

## V. CONCLUSION

We synthesized (using a solid-solution approach) and investigated the dielectric and piezoelectric properties of the chiral perovskite *R*-CYHEAPbI<sub>3</sub>. Different theoretical models, including the Maxwell-Wagner equivalent circuit model, the universal power law, the Havriliak-Negami model, and the Kohlrausch-Williams-Watts model, were used to fit experimental results from dielectric spectroscopy. We observed that the dc conductivity was nearly constant between 353 and 373 K, while the dc conductivity increased with temperature below and above this range. A phase change from ferroelectric to paraelectric might be ascribed to this anomaly in the dc conductivity. Remarkably, we found that the activation energy was 0.85( $\pm$ 0.04) eV in the low-temperature region (below the phase transition region) and 0.90( $\pm$ 0.04) eV in the high-temperature region (above the phase transition region), but the phase transition region exhibited a very low activation energy of 0.09( $\pm$ 0.04) eV. The activation energy derived from the relaxation time using the HN and KWW models was consistent with the values obtained using dc conductivity. The consistency of ionic conduction and relaxation phenomena for *R*-CYHEAPbI<sub>3</sub> at various temperatures was shown by the scaling of temperature-dependent conductivity and electric modulus spectra into a single master

curve. Chiral *R*-CYHEAPbI<sub>3</sub> exhibited a saturation polarization of 0.01  $\mu$ C/cm<sup>2</sup> under an applied electric field of 4 kV/cm and a piezoelectric constant ( $d_{33}$ ) of 36 pm/V under the maximum applied bias voltage of 10 V. Finally, we fabricated a composite film of PVDF and 3-wt% *R*-CYHEAPbI<sub>3</sub> chiral perovskite loaded in the PVDF matrix film to demonstrate its utility as a mechanical energy harvester from biomechanical motion.

## ACKNOWLEDGMENT

Funding from the MoE-STARS, Government of India, under Project No. MoE-STARS/STARS-1/231 is gratefully acknowledged. We also thank the Central Instrumentation Facility at IIT Gandhinagar for facilitating several measurements. A.G. received support from a Raja Ramanna Fellowship from the Department of Atomic Energy, Government of India.

- 
- [1] A. G. Ricciardulli, S. Yang, J. H. Smet, and M. Saliba, Emerging perovskite monolayers, *Nat. Mater.* **20**, 1325 (2021).
  - [2] H. Y. Zhang, Z. X. Zhang, X. G. Chen, X. J. Song, Y. Zhang, and R. G. Xiong, Large electrostrictive coefficient in a two-dimensional hybrid perovskite ferroelectric, *J. Am. Chem. Soc.* **143**, 1664 (2021).
  - [3] R. Chaurasia, K. Asokan, K. Kumar, and A. K. Pramanik, Low-temperature ferromagnetism in perovskite SrIrO<sub>3</sub> films, *Phys. Rev. B* **103**, 064418 (2021).
  - [4] S. Mondal, S. Maiti, T. Paul, A. Sahoo, S. Bhattacharjee, N. S. Das, and K. K. Chattopadhyay, All-inorganic halide perovskite tuned robust mechanical-energy harvester: Self driven posture monitor and power source for portable electronics, *Appl. Mater. Today* **26**, 101385 (2022).
  - [5] P. Zhou, H. Chen, Y. Chao, Q. Zhang, W. Zhang, F. Lv, L. Gu, Q. Zhao, N. Wang, J. Wang, *et al.*, Single-atom Pt-I<sub>3</sub> sites on all-inorganic Cs<sub>2</sub>SnI<sub>6</sub> perovskite for efficient photocatalytic hydrogen production, *Nat. Commun.* **12**, 1 (2021).
  - [6] T. Paul, B. K. Chatterjee, P. Bairi, S. Maiti, N. Besra, B. K. Das, S. Thakur, and K. K. Chattopadhyay, Electrochemical performance of 3D network CsPbBr<sub>3</sub> perovskite anode for Li-ion batteries: Experimental venture with theoretical expedition, *J. Phys. Chem. C* **125**, 16892 (2021).
  - [7] N. H. Makani, M. Singh, T. Paul, A. Sahoo, J. Nama, S. Sharma, and R. Banerjee, Shape dependent photocatalytic CO<sub>2</sub> reduction using lead-free bimetallic CsAgBr<sub>2</sub> halide perovskite, *J. Electroanal. Chem.* **920**, 116583 (2022).
  - [8] T. Paul, P. K. Sarkar, S. Maiti, A. Sahoo, and K. K. Chattopadhyay, Solution-processed light induced multilevel non-volatile wearable memory device based on CsPb<sub>2</sub>Br<sub>5</sub> perovskite, *Dalton Trans.* **51**, 3864 (2022).
  - [9] M. Singh, J. Nama, T. Paul, N. H. Makani, A. Sahoo, S. Sharma, and R. Banerjee, Photoelectrochemically induced CO<sub>2</sub> reduction using halide-tunable lead-free perovskites, *ACS Appl. Energy Mater.* **6**, 3566 (2023).



- [10] Y. Hu, F. Florio, Z. Chen, W. A. Phelan, M. A. Siegler, Z. Zhou, Y. Guo, R. Hawks, J. Jiang, J. Feng, *et al.*, A chiral switchable photovoltaic ferroelectric 1D perovskite, *Sci. Adv.* **6**, eaay4213 (2020).
- [11] L. Xu, X. Wang, W. Wang, M. Sun, W. J. Choi, J. Y. Kim, C. Hao, S. Li, A. Qu, M. Lu, *et al.*, Enantiomer-dependent immunological response to chiral nanoparticles, *Nature* **601**, 366 (2022).
- [12] Y. Dang, X. Liu, B. Cao, and X. Tao, Chiral halide perovskite crystals for optoelectronic applications, *Matter* **4**, 794 (2021).
- [13] H. Lee, M. J. Huttunen, K. J. Hsu, M. Partanen, G. Y. Zhuo, M. Kauranen, and S. W. Chu, Chiral imaging of collagen by second-harmonic generation circular dichroism, *Biomed. Opt. Express* **4**, 909 (2013).
- [14] J. Yin, Y. Cao, Y. H. Li, S. K. Liao, L. Zhang, J. G. Ren, W. Q. Cai, W. Y. Liu, B. Li, H. Dai, *et al.*, Satellite-based entanglement distribution over 1200 kilometers, *Science* **356**, 1140 (2017).
- [15] J. Xiao, H. Zheng, R. Wang, Y. Wang, and S. Hou, Spin-polarized excitons and charge carriers in chiral metal halide semiconductors, *J. Mater. Chem. A* **10**, 19367 (2022).
- [16] D. G. Billing and A. Lemmerer, *Acta Crystallogr., Sect. E: Struct. Rep. Online* **59**, m381 (2003).
- [17] D. G. Billing and A. Lemmerer, Synthesis and crystal structures of inorganic–organic hybrids incorporating an aromatic amine with a chiral functional group, *CrystEngComm* **8**, 686 (2006).
- [18] J. Ahn, E. Lee, J. Tan, W. Yang, B. Kim, and J. Moon, A new class of chiral semiconductors: Chiral-organic-molecule-incorporating organic–inorganic hybrid perovskites, *Mater. Horiz.* **4**, 851 (2017).
- [19] X. Wang, J. Hao, J. Cheng, J. Li, J. Miao, R. Li, Y. Li, J. Li, Y. Liu, X. Zhu, *et al.*, Chiral CdSe nanoplatelets as an ultrasensitive probe for lead ion sensing, *Nanoscale* **11**, 9327 (2019).
- [20] J. Tian, G. Adamo, H. Liu, M. Klein, S. Han, H. Liu, and C. Soci, Optical Rashba effect in a light-emitting perovskite metasurface, *Adv. Mater.* **34**, 2109157 (2022).
- [21] Y. Cai, Y. Hu, Z. Chen, J. Jiang, L. Zhang, Y. Guo, S. Pendse, R. Jia, J. Zhang, X. Ma, *et al.*, van der Waals Ferroelectric Halide Perovskite Artificial Synapse, *Phys. Rev. Appl.* **18**, 014014 (2022).
- [22] Y. Cai, L. Zhang, J. Jiang, Y. Hu, Z. Chen, R. Jia, C. Sun, J. Shi, and A. Van Der Waals, Photo-ferroelectric synapse, *Adv. Electron. Mater.* **8**, 2200326 (2022).
- [23] J. Islam and A. K. M. Hossain, Semiconducting to metallic transition with outstanding optoelectronic properties of CsSnCl<sub>3</sub> perovskite under pressure, *Sci. Rep.* **10**, 1 (2020).
- [24] P. Maji, A. Ray, P. Sadhukhan, S. Chatterjee, and S. Das, Study on charge transfer mechanism and dielectric relaxation of cesium lead bromide (CsPbBr<sub>3</sub>), *J. Appl. Phys.* **124**, 124102 (2018).
- [25] S. Shahrokhi, W. Gao, Y. Wang, P. R. Anandan, M. Z. Rahaman, S. Singh, D. Wang, C. Cazorla, G. Yuan, J.-M. Liu, *et al.*, Emergence of ferroelectricity in halide perovskites, *Small Methods* **4**, 2000149 (2020).
- [26] See the Supplemental Material at <http://link.aps.org/supplemental/10.1103/PhysRevApplied.20.034024> for differential scanning calorimetry, XPS survey scan, piezoresponse loop, parameters estimated from fitting of the Nyquist plot using the Maxwell-Wagner equivalent circuit model, parameter values obtained from fitting the power-law exponent ( $s$ ) using the OLPT model and CBH model, a comparison of the piezoresponse of various halide perovskites, and a performance comparison of *R*-CYHEAPbI<sub>3</sub>–polymer-composite-based nanogenerator with others.
- [27] S. Chen, T. W. Goh, D. Sabba, J. Chua, N. Mathews, C. H. A. Huan, and T. C. Sum, Energy level alignment at the methylammonium lead iodide/copper phthalocyanine interface, *APL Mater.* **2**, 081512 (2014).
- [28] Z. Hawash, S. R. Raga, D. Y. Son, L. K. Ono, N. G. Park, and Y. Qi, Interfacial modification of perovskite solar cells using an ultrathin MAI layer leads to enhanced energy level alignment, efficiencies, and reproducibility, *J. Phys. Chem. Lett.* **8**, 3947 (2017).
- [29] S. Chen, A. Solanki, J. Pan, and T. C. Sum, Compositional and morphological changes in water-induced early-stage degradation in lead halide perovskites, *Coatings* **9**, 535 (2019).
- [30] T. Paul, S. Maiti, N. Besra, B. K. Chatterjee, B. K. Das, S. Thakur, S. Sarkar, N. S. Das, and K. K. Chattopadhyay, Tailored CsPbX<sub>3</sub> nanorods for electron-emission nanodevices, *ACS Appl. Nano Mater.* **9**, 5942 (2019).
- [31] S. Pujaru, P. Maji, P. Sadhukhan, A. Ray, B. Ghosh, and S. Das, Dielectric relaxation and charge conduction mechanism in mechanochemically synthesized methylammonium bismuth iodide, *J. Mater. Sci. Mater. Electron.* **31**, 8670 (2020).
- [32] G. R. Gajula, L. R. Buddiga, K. N. Chidambara Kumar, and M. Dasari, Study on electric modulus, complex modulus and conductivity properties of Nb/Sm, Gd doped barium titanate-lithium ferrite ceramic composites, *Res. Phys.* **17**, 103076 (2020).
- [33] P. Gupta, L. K. Meher, and R. N. P. Choudhary, Structural, dielectric, impedance and modulus spectroscopy of BiLa<sub>2</sub>TiVO<sub>9</sub> ceramic, *Appl. Phys. A* **126**, 1 (2020).
- [34] A. Sahoo, T. Paul, S. Maiti, and R. Banerjee, Temperature-dependent dielectric properties of CsPb<sub>2</sub>Br<sub>5</sub>: A 2D inorganic halide perovskite, *Nanotechnology* **33**, 195703 (2022).
- [35] P. Pal and A. Ghosh, Three-Dimensional CsPbCl<sub>3</sub> Perovskite Anode for Quasi-Solid-State Li-Ion and Dual-Ion Batteries: Mechanism of Li<sup>+</sup> Conversion Process in Perovskite, *Phys. Rev. Appl.* **14**, 064010 (2020).
- [36] J. Liu, C. G. Duan, W. N. Mei, R. W. Smith, and J. R. Hardy, Dielectric properties and Maxwell-Wagner relaxation of compounds ACu<sub>3</sub>Ti<sub>4</sub>O<sub>12</sub> ( $A = \text{Ca}, \text{Bi}_{2/3}, \text{Y}_{2/3}, \text{La}_{2/3}$ ), *J. Appl. Phys.* **98**, 093703 (2005).
- [37] N. H. Makani, A. Sahoo, P. Pal, T. Paul, L. S. Tanwar, M. Singh, A. Ghosh, and R. Banerjee, Onset of vacancy-mediated high activation energy leads to large ionic conductivity in two-dimensional layered Cs<sub>2</sub>PbI<sub>2</sub>Cl<sub>2</sub> Ruddlesden-Popper halide perovskite, *Phys. Rev. Mater.* **6**, 115002 (2022).
- [38] C. R. Cena, A. K. Behera, and B. Behera, Structural, dielectric, and electrical properties of lithium niobate microfibers, *J. Adv. Ceram.* **5**, 84 (2016).
- [39] C. G. Koops, On the dispersion of resistivity and dielectric constant of some semiconductors at audio frequencies, *Phys. Rev.* **83**, 121 (1951).

- [40] P. Sengupta, P. Sadhukhan, A. Ray, R. Ray, S. Bhatlacharyya, and S. Das, Temperature and frequency dependent dielectric response of  $C_3H_7NH_3PbI_3$ : A new hybrid perovskite, *J. Appl. Phys.* **127**, 204103 (2020).
- [41] M. Ahmad, M. A. Rafiq, K. Rasool, Z. Imran, and M. M. Hasan, Dielectric and transport properties of bismuth sulfide prepared by solid state reaction method, *J. Appl. Phys.* **113**, 043704 (2013).
- [42] D. K. Pradhan, P. Misra, V. S. Puli, S. Sahoo, D. K. Pradhan, and R. S. Katiyar, Studies on structural, dielectric, and transport properties of  $Ni_{0.65}Zn_{0.35}Fe_2O_4$ , *J. Appl. Phys.* **115**, 243904 (2014).
- [43] L. Liu, D. Shi, H. Yanmin, S. Wu, X. Chen, L. Fang, and C. Hu, Quantitative description of the diffuse phase transition of BNT-NKN ceramics, *Ferroelectrics* **432**, 65 (2012).
- [44] J. Liu, C. G. Duan, W. G. Yin, W. N. Mei, R. W. Smith, and J. R. Hardy, Dielectric permittivity and electric modulus in  $Bi_2Ti_4O_{11}$ , *J. Chem. Phys.* **119**, 2812 (2003).
- [45] X. Z. Zuo, J. Yang, B. Yuan, D. P. Song, X. W. Tang, K. J. Zhang, X. B. Zhu, W. H. Song, J. M. Dai, and Y. P. Sun, Magnetic, dielectric properties, and scaling behaviors of Aurivillius compounds  $Bi_{6-x/3}Fe_2Ti_{3-2x}(WCo)_xO_{18}$  ( $0 \leq x \leq 0.15$ ), *J. Appl. Phys.* **117**, 114101 (2015).
- [46] K. Funke and R. Hoppe, Jump-relaxation model yields Kohlrausch-Williams-Watts behaviour, *Solid State Ion.* **40**, 200 (1990).
- [47] A. K. Jonscher, The ‘universal’ dielectric response, *Nature* **267**, 673 (1977).
- [48] M. B. Bechir and A. B. Rhaïem, Structural phase transition, vibrational analysis, ionic conductivity and conduction mechanism studies in an organic-inorganic hybrid crystal:  $[N(CH_3)_3H]_2CdCl_4$ , *J. Solid State Chem.* **296**, 122021 (2021).
- [49] A. K. Jonscher, *Dielectric Relaxation in Solids* (Chelsea Dielectric Press, London, 1983).
- [50] L. Murawski, C. H. Chung, and J. D. Mackenzie, Electrical properties of semiconducting oxide glasses, *J. Non. Cryst. Solids* **32**, 91 (1979).
- [51] S. R. Elliott, ac conduction in amorphous chalcogenide and pnictide semiconductors, *Adv. Phys.* **36**, 135 (1987).
- [52] K. B. Brahim, A. Oueslati, F. Hlel, and M. Gargouri, Synthesis, structural characterization and electrical conduction mechanism of the new organic-inorganic complex:  $[(C_3H_7)_4N]FeCl_4$ , *Mater. Res. Bull.* **118**, 110505 (2019).
- [53] I. G. Austin and N. F. Mott, Polarons in crystalline and non-crystalline materials, *Adv. Phys.* **18**, 41 (1969).
- [54] A. R. Long, Frequency-dependent loss in amorphous semiconductors, *Adv. Phys.* **31**, 553 (1982).
- [55] A. Ghosh, Frequency-dependent conductivity in bismuth vanadate glassy semiconductors, *Phys. Rev. B* **41**, 1479 (1990).
- [56] P. Thongbai, S. Tangwanchaoen, T. Yamwong, and S. Maensiri, Dielectric relaxation and dielectric response mechanism in (Li, Ti)-doped NiO ceramics, *J. Phys.: Condens. Matter* **20**, 395227 (2008).
- [57] N. K. Tailor, N. Parikh, P. Yadav, and S. Satapathi, Dielectric relaxation and polaron hopping in  $Cs_2AgBiBr_6$  halide double perovskites, *J. Phys. Chem. C* **126**, 10199 (2022).
- [58] S. Havriliak and S. Negami, A complex plane representation of dielectric and mechanical relaxation processes in some polymers, *Polymer* **8**, 161 (1967).
- [59] G. Williams and D. C. Watts, Non-symmetrical dielectric relaxation behaviour arising from a simple empirical decay function, *Trans. Faraday Soc.* **66**, 80 (1970).
- [60] K. L. Ngai, Properties of the constant loss in ionically conducting glasses, melts, and crystals, *J. Chem. Phys.* **110**, 10576 (1999).
- [61] F. S. Howell, R. A. Bose, P. B. Macedo, and C. T. Moynihan, Electrical relaxation in a glass-forming molten salt, *J. Phys. Chem.* **78**, 639 (1974).
- [62] G. C. Psarras, E. Manolakaki, and G. M. Tsangaris, Dielectric dispersion and ac conductivity in—iron particles loaded—polymer composites, *Composites, Part A* **34**, 1187 (2003).
- [63] A. Ghosh and A. Pan, Scaling of the Conductivity Spectra in Ionic Glasses: Dependence on the Structure, *Phys. Rev. Lett.* **84**, 2188 (2000).
- [64] R. Pandey, S. B. Gangadhar, S. Grover, S. K. Singh, A. Kadam, S. Ogale, U. V. Waghmare, V. Ramgopal Rao, and D. Kabra, Microscopic origin of piezoelectricity in lead-free halide perovskite: Application in nanogenerator design, *ACS Energy Lett.* **4**, 1004 (2019).
- [65] J. Xiao, W. L. Ong, Z. Guo, G. W. Ho, and K. Zeng, Resistive switching and polarization reversal of hydrothermal method-grown undoped zinc oxide nanorods by using scanning probe microscopy techniques, *ACS Appl. Mater. Interfaces* **7**, 11412 (2015).
- [66] M. Singh, T. Paul, P. Pal, A. Sahoo, L. S. Tanwar, N. H. Makani, A. Ghosh, and R. Banerjee, High ionic conduction and polarity-induced piezoresponse in layered bimetallic  $Rb_4Ag_2BiBr_9$  single crystals, *J. Phys. Chem. C* **126**, 21810 (2022).
- [67] A. Sahoo, T. Paul, N. H. Makani, S. Maiti, and R. Banerjee, High piezoresponse in low-dimensional inorganic halide perovskite for mechanical energy harvesting, *Sustainable Energy Fuels* **6**, 4484 (2022).
- [68] S. Huang, G. Tang, H. Huang, X. G. Wu, P. Zhou, L. Zou, L. Xie, J. Deng, X. Wang, H. Zhong, *et al.*, Enhanced piezo-response in copper halide perovskites based PVDF composite films, *Sci. Bull.* **63**, 1254 (2018).
- [69] Q. Zhang, A. Solanki, K. Parida, D. Giovanni, M. Li, T. L. Jansen, M. S. Pshenichnikov, and T. C. Sum, Tunable ferroelectricity in Ruddlesden-Popper halide perovskites, *ACS Appl. Mater. Interfaces* **11**, 13523 (2019).
- [70] J. Xiao, J. Chang, B. Li, F. H. Isikgor, D. Wang, Z. Fan, Z. Lin, J. Ouyang, K. Zeng, and J. Chen, Room temperature ferroelectricity of hybrid organic-inorganic perovskites with mixed iodine and bromine, *J. Mater. Chem. A* **6**, 9665 (2018).
- [71] Z. X. Wang, H. Zhang, F. Wang, H. Cheng, W. H. He, Y. H. Liu, X. Q. Huang, and F. P. Li, Superior transverse piezoelectricity in a halide perovskite molecular ferroelectric thin film, *J. Am. Chem. Soc.* **142**, 12857 (2020).
- [72] J. Nie, L. Zhu, W. Zhai, A. Berbille, L. Li, and Z. L. Wang, Flexible piezoelectric nanogenerators based on P(VDF-TrFE)/CsPbBr<sub>3</sub> quantum dot composite films, *ACS Appl. Electron. Mater.* **3**, 2136 (2021).
- [73] S. K. Si, S. Paria, S. K. Karan, S. Ojha, A. K. Das, A. Maitra, A. Bera, L. Halder, A. De, and B. B. Khatua,



- In situ*-grown organo-lead bromide perovskite-induced electroactive  $\gamma$ -phase in aerogel PVDF films: An efficient photoactive material for piezoelectric energy harvesting and photodetector applications, *Nanoscale* **12**, 7214 (2020).
- [74] R. Ding, H. Liu, X. Zhang, J. Xiao, R. Kishor, H. Sun, B. Zhu, G. Chen, F. Gao, X. Feng, *et al.*, Flexible piezoelectric nanocomposite generators based on formamidinium lead halide perovskite nanoparticles, *Adv. Funct. Mater.* **26**, 7708 (2016).
- [75] V. Jella, S. Ippili, J. H. Eom, J. Choi, and S. G. Yoon, Enhanced output performance of a flexible piezoelectric energy harvester based on stable MAPbI<sub>3</sub>-PVDF composite films, *Nano Energy* **53**, 46 (2018).
- [76] S. Mondal, T. Paul, S. Maiti, B. K. Das, and K. K. Chattopadhyay, Human motion interactive mechanical energy harvester based on all inorganic perovskite-PVDF, *Nano Energy* **74**, 104870 (2020).
- [77] A. Sultana, M. M. Alam, P. Sadhukhan, U. K. Ghorai, S. Das, T. R. Mirdya, and D. Mandal, Organo-lead halide perovskite regulated green light emitting poly(vinylidene fluoride) electrospun nanofiber mat and its potential utility for ambient mechanical energy harvesting application, *Nano Energy* **49**, 380 (2018).